Received: 22 March 2020 | Revised: 4 October 2020 | Accepted: 5 October 2020

DOI: 10.1002/nme.6562

RESEARCH ARTICLE

WILEY

Displacement-based and hybrid formulations of zero-thickness mortar/interface elements for unmatched meshes, with application to fracture mechanics

Miguel de Francisco | **Ignacio Carol**

Division of Geotechnical Engineering and Geo-Sciences, ETSECCPB (School of Civil Engineering), UPC (Technical Univ. of Catalonia), Barcelona, Spain

Correspondence
Ignacio Carol, ETSECCPB-UPC, Jordi Girona 1-3, Edif. D2 08034 Barcelona, Spain.
Email: ignacio.carol@upc.edu

Funding information
Agència de Gestió d'Ajuts Universitaris i de Recerca, Grant/Award Numbers: 2017SGR-1153, FI-2015; Ministerio de Educación, Cultura y Deporte, Grant/Award Numbers: BIA2016-76543-R, FPU15/02577

Abstract

The present article develops two formulations of zero-thickness mortar/interface finite elements for unmatched meshes, which are implemented in a unified theoretical framework. The first one is displacement-based and may be considered a natural extension of the traditional zero-thickness interface element to the case of unmatched meshes on each side of the discontinuity. The other one is hybrid, with an interpolation of stress tractions along the contact surface, which coexists with the standard displacement interpolations of the continuum surfaces in contact. The hybrid formulation shares some features with mortar formulations found in the literature of contact-friction, and turns out fully equivalent to the displacement-based in the particular case of matched nodes and uniform, linear elastic behavior. Flow chart diagrams for the numerical implementation are also presented and discussed, as well as some examples of application.

KEYWORDS

hybrid elements, mortar method, non(conforming/matching) meshes, zero-thickness interfaces

1 | INTRODUCTION

Zero-thickness interface elements, also known as cohesive elements, were first proposed in the late 1960s in the geomechanical literature[1,2] and since then they have been a very useful tool for the small-strain quasi-static representation of discontinuities, fractures, or contacts between different materials in all fields of Engineering including also fluid-filled discontinuities, for example, References [3–9]. However, one essential limitation of their original formulation is that nodes on each side of the discontinuity have to coincide in location. This means that meshes of the continuum on both sides of the interface surface have to match each other, which may be a natural condition to satisfy in some cases, but in many others, it may be too restrictive. Consider, for instance, complex geometries including different subdomains, which may be subject to different type of analysis requiring different mesh sizes (e.g., a hydrocarbon reservoir where the flow analysis is performed, which is inserted in a much larger domain subject to mechanical analysis).[10] The condition of matched meshes across the discontinuities may also be too restrictive in the case of meshes initially matched, that may become unmatched due to large opening/sliding of the discontinuities, such as for instance may happen in the analysis of landslides or simulation of geotectonics processes.[11,12] And probably, the most paradigmatic case of unmatched meshes is the

general contact/friction problem between two bodies, which have been discretized with independent meshes, and it is not known a priori what part of the surfaces from each body will get in contact with the other.

Focusing on the case that the meshes on the continuum on both sides of the discontinuity (or bodies in contact) are preestablished independently, and that the geometry of the contact surface has been determined, one successful approach to formulate such contact is that of mortar elements. The terminology of mortar element was coined in the context of spectral discretization of domain decomposition methods,[13,14] and the concept was later extended to the FEM analysis,[15] where it was shown to preserve the optimal convergence ratio and fulfil the Babuska–Brezzi condition,[16] and then to large-deformation contact-friction problems.[17–20] Initially, mortar elements were formulated on the basis of Lagrange multipliers, assigning arbitrarily the roles of master and slave surfaces, which in the usual mortar terminology are called mortar and nonmortar surfaces respectively. The latter is the surface over which the Lagrange multipliers are interpolated. Later, some mortar formulations were also developed on the basis of the penalty approach,[18] and used an intermediate mortar surface,[21] which opened the door to a more symmetric treatment of both contact surfaces. However, mortar formulations have been generally developed in the context of contact-friction problems and dynamic analysis, with no trivial connection to the formulation of zero-thickness elements, in spite of physical and conceptual similarities.

On the other hand, literature on interface or cohesive elements seems to have focused mainly on other aspects such as elimination of the interface prepeak elastic stiffness, either via progressive interface insertion with topology changes in fragmentation studies,[22,23] or via discontinuous Galerkin approach with automatic switch to traditional interfaces as the strength limit is exceeded.[24,25] The case of interface (cohesive) elements with unmatched meshes seems to have been tackled only recently[26] with the formulation of a cohesive contact between two solid bodies with independent meshes. In that formulation, the interpolation is purely displacement-based (no other interpolations except the displacements of the surfaces of the two bodies), and the cohesive elements are assumed to coincide with the discretization of one of the two bodies arbitrarily, something reminiscent of the master/slave concept in contact mechanics.

In the present study, efforts have been directed to generalize the unmatched interface formulation by incorporating some additional concepts from mortar approaches in the contact literature: (1) the mortar/interface elements proposed are not arbitrarily attached to any of the two surfaces in contact, but they are defined as the smallest segments resulting from projection of the two surfaces on an independent "mid-distance" mortar surface and (2) the formulation is developed in two flavors, a first one based on displacement interpolations exclusively ("displacement-based") and a second one based on a dual interpolation: displacements for the side surfaces and stress tractions for the contact itself ("hybrid formulation"). The displacement-based formulation turns out the natural extension, to the case of unmatched meshes, of the traditional displacement-based formulation of zero-thickness interface elements. By contrast, the hybrid formulation constitutes a related but novel formulation, which is developed first in the case of unmatched meshes, and then is particularized for coincident meshes to obtain an (also novel) hybrid formulation of the zero-thickness interface element.

One of the advantages of the approach followed is in terms of the constitutive behavior, since the resulting mortar elements may incorporate any existing constitutive model for classical zero-thickness interface elements. This may be particularly useful in the case of fracturing solids or geomechanical domains with existing fractures or developing discontinuities. In this particular study, the elastoplastic geomechanical model for existing discontinuities,[27] or the for normal/shear cracking model based in fracture mechanics concepts, both in elastoplastic version[28,29] or viscoplastic version,[30] have been used in some of the examples presented.

The article is structured as follows: after this Introduction, a brief summary of the traditional formulation of zero-thickness interface elements is presented in Section 2; the displacement-based formulation of the mortar/interface element is developed in Section 3, and the new hybrid formulation in Section 4. Section 5 is focused on the particular case of matched nodes and constant linear elasticity, in which it is proven that both displacement-based and hybrid formulations turn out fully equivalent to the traditional formulation of zero-thickness interface elements. Section 6 is devoted to the comparison of both formulations in the general case and to numerical implementation aspects. Various examples of application are included in Section 7 and, finally, Section 8 includes the main conclusions of the work presented.

2 | STANDARD FORMULATION OF ZERO-THICKNESS INTERFACE ELEMENTS

This section includes a brief summary/reminder of the traditional zero-thickness interface formulation, since this is the departure point to the mortar element formulations developed in subsequent sections. Figure 1 shows a linear interface element composed of two faces with two nodes per face. The two faces are, at the same time, faces of two continuum

FIGURE 1 Geometry of traditional zero-thickness interface element

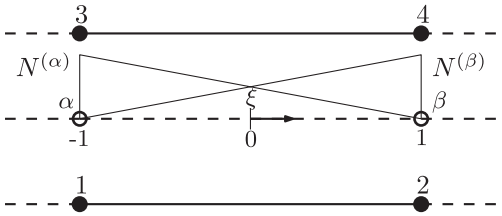

elements, the contact of which is precisely represented by the interface. In the figure, the two element faces are depicted at a distance from each other for representation purposes only, since locations the two faces are generally coincident. A midplane surface is defined at mid-distance between the two faces. The midplane surface is parametrized via a local coordinate ξ varying from $\xi = -1$ (for midpoint α between nodes 1 and 3 at the left end of the element) to $\xi = +1$ (for point β in between nodes 2 and 4 at the right end of the element). Two shape functions are defined along the midplane surface, $N^{(\alpha)}(\xi)$ and $N^{(\beta)}(\xi)$, which are also represented in Figure 1.

The absolute displacement of a point on the upper face is obtained by interpolation between values at nodes 3 and 4, with functions $N^{(\alpha)}(\xi)$ and $N^{(\beta)}(\xi)$, and similarly for any point on the lower face in between nodes 1 and 2. The *x,y* relative displacements of a point with local coordinate ξ along the midplane surface, $\boldsymbol{r}^{xy}(\xi)$, is defined as the displacement difference between the upper and lower faces and is also given by the same interpolation, leading to:

$$\boldsymbol{r}^{xy}(\xi) = \left[-\mathbf{N}^{(\alpha)}(\xi) \middle| -\mathbf{N}^{(\beta)}(\xi) \middle| \ \mathbf{N}^{(\alpha)}(\xi) \middle| \ \mathbf{N}^{(\beta)}(\xi) \right] \begin{bmatrix} \boldsymbol{u}_1 \\ \boldsymbol{u}_2 \\ \boldsymbol{u}_3 \\ \boldsymbol{u}_4 \end{bmatrix} = \mathbf{N}^{el}(\xi)\, \boldsymbol{u}^{el}, \tag{1}$$

where $\mathbf{N}^{el}(\xi)$ is the shape function matrix composed of four submatrices involving

$$\mathbf{N}^{(\alpha)}(\xi) = N^{(\alpha)}(\xi)\, \mathbf{I},\ \mathbf{N}^{(\beta)}(\xi) = N^{(\beta)}(\xi)\, \mathbf{I}, \tag{2}$$

and $\boldsymbol{u}_1$, $\boldsymbol{u}_2$, $\boldsymbol{u}_3$, $\boldsymbol{u}_4$ are the standard nodal displacements in Cartesian axes, which are gathered in column vector $\boldsymbol{u}^{el}$. Multiplication by rotation matrix leads to the relative displacements in local (n,t) axes:

$$\boldsymbol{r}(\xi) = \mathbf{R}(\xi)\, \boldsymbol{r}^{xy}(\xi) = \left[\mathbf{B}^{(1)}(\xi) \middle| \ \mathbf{B}^{(2)}(\xi) \middle| \ \mathbf{B}^{(3)}(\xi) \ \middle| \ \mathbf{B}^{(4)}(\xi) \right] \begin{bmatrix} \boldsymbol{u}_1 \\ \boldsymbol{u}_2 \\ \boldsymbol{u}_3 \\ \boldsymbol{u}_4 \end{bmatrix} = \mathbf{B}^{el}(\xi)\, \boldsymbol{u}^{el}, \tag{3}$$

where $\mathbf{B}^{el}(\xi)$ is the classical "B" matrix composed, in this case, of the four submatrices.

$$\mathbf{B}^{(1)} = -\mathbf{R}\mathbf{N}^{(\alpha)},\ \mathbf{B}^{(2)} = -\mathbf{R}\mathbf{N}^{(\beta)},\ \mathbf{B}^{(3)} = \mathbf{R}\mathbf{N}^{(\alpha)},\ \mathbf{B}^{(4)} = \mathbf{R}\mathbf{N}^{(\beta)}. \tag{4}$$

The most general form of linear constitutive law is now considered:

$$\boldsymbol{t} = \boldsymbol{D}\, \boldsymbol{r} + \boldsymbol{t}_0, \tag{5}$$

where $\boldsymbol{t}$ is the stress traction vector containing normal and shear stress traction components, $\boldsymbol{D}$ is the constitutive stiffness matrix, and $\boldsymbol{t}_0$ is an initial stress vector which, depending on the context, may have a physical meaning (e.g., in case of initial prescribed deformations $\boldsymbol{r}_0$, initial stress are $\boldsymbol{t}_0 = -\boldsymbol{D}\boldsymbol{r}_0$). By introducing the relative displacements (3) into constitutive relation (5), one obtains the expression of the contact stress tractions along the mortar surface in terms of nodal displacements:

$$\boldsymbol{t} = \boldsymbol{D}\mathbf{B}^{el}(\xi)\boldsymbol{u}^{el} + \boldsymbol{t}_0. \tag{6}$$

The element matrix formulation is obtained by application of the PVW. Considering a virtual variation of the nodal displacements $\delta \boldsymbol{u}^{el}$ and the (kinematically compatible) virtual relative displacements all along the mortar surface $\delta \boldsymbol{r}$, as well as a field of mortar surface stress tractions $\boldsymbol{t}$ and the (statically in equilibrium) corresponding nodal force vector $\boldsymbol{F}^{el}$, one can write

$$(\delta \boldsymbol{u}^{el})^T \boldsymbol{F}^{el} = \int_S (\delta \boldsymbol{r})^T \boldsymbol{t}\, dS, \tag{7}$$

where superindex $(.)^T$ stands for transposed, and the integral domain is the mortar surface defined by the local coordinate range $\xi = -1$ to 1. Replacing the relative displacement vector $\boldsymbol{r}$ with expression (3) and taking nodal vectors out of the integral, leads to the standard format of the weak equilibrium equation

$$\boldsymbol{F}^{el} = \int_S (\mathbf{B}^{el})^T \boldsymbol{t}\, dS. \tag{8}$$

In order to obtain the element stiffness matrix and initial force vector, the stress traction vector $\boldsymbol{t}$ is replaced with Equation (6), which leads to the final expressions

$$\boldsymbol{F}^{el} = \mathbf{K}^{el}\, \boldsymbol{u}^{el} + \boldsymbol{F}_0^{el}, \tag{9}$$

$$\mathbf{K}^{el} = \int_S (\mathbf{B}^{el})^T \boldsymbol{D} \mathbf{B}^{el}\, dS,\ \boldsymbol{F}_0^{el} = \int_S (\mathbf{B}^{el})^T \boldsymbol{t}_0 dS. \tag{10}$$

Previous equations may also be rephrased in an alternative format,[2] which is more convenient for comparison in later sections of the article. This is achieved by decomposing the overall matrix $\mathbf{B}^{el}(\xi)$ (3) in two submatrices corresponding to the nodes of each of the surfaces A and B, and realizing that due to (4) and except for a sign, the two submatrices turn out equal to a "midplane B" matrix $\mathbf{B}_{MP}(\xi)$:

$$\begin{aligned} \mathbf{B}^{el}(\xi) &= \left[\ \mathbf{B}_A(\xi)\ \middle|\ \mathbf{B}_B(\xi)\right], \\ \mathbf{B}_A(\xi) &= \left[\mathbf{B}^{(1)}(\xi)\ \middle|\ \mathbf{B}^{(2)}(\xi)\right] = \left[-\mathbf{R}\mathbf{N}^{(\alpha)}(\xi)\ \middle|\ -\mathbf{R}\mathbf{N}^{(\beta)}(\xi)\right] = -\mathbf{B}_{MP}(\xi), \\ \mathbf{B}_B(\xi) &= \left[\mathbf{B}^{(3)}(\xi)\ \middle|\ \mathbf{B}^{(4)}(\xi)\ \right] = \left[\mathbf{R}\mathbf{N}^{(\alpha)}(\xi)\ \middle|\ \mathbf{R}\mathbf{N}^{(\beta)}(\xi)\right] = \mathbf{B}_{MP}(\xi). \end{aligned} \tag{11}$$

This may be introduced into (10) to obtain:

$$\mathbf{K}^{el} = \begin{bmatrix} \mathbf{k}_{MP} & -\mathbf{k}_{MP} \\ -\mathbf{k}_{MP} & \mathbf{k}_{MP} \end{bmatrix} = \begin{bmatrix} -\mathbf{I}_4 \\ \mathbf{I}_4 \end{bmatrix} \mathbf{k}_{MP} [\,-\mathbf{I}_4 |\ \mathbf{I}_4], \quad \boldsymbol{F}_0^{el} = \begin{bmatrix} -\boldsymbol{f}_0^{el} \\ \boldsymbol{f}_0^{el} \end{bmatrix} = \begin{bmatrix} -\mathbf{I}_4 \\ \mathbf{I}_4 \end{bmatrix} \boldsymbol{f}_0^{el}, \tag{12}$$

in which $\mathbf{k}_{MP}$ is the "intrinsic" midplane stiffness matrix and $\boldsymbol{f}_0^{el}$ is the initial force vector, both in terms of relative degrees of freedom and pairs of forces:

$$\mathbf{k}_{MP} = \int_S (\mathbf{B}_{MP})^T \boldsymbol{D}\, \mathbf{B}_{MP}\, dS,\ \boldsymbol{f}_0^{el} = \int_S (\mathbf{B}_{MP})^T \boldsymbol{t}_0 dS \tag{13}$$

and $\mathbf{I}_4$ is the 4×4 identity matrix:

$$\mathbf{I}_4 = \begin{bmatrix} \mathbf{I} & 0 \\ 0 & \mathbf{I} \end{bmatrix}. \tag{14}$$

3 | DISPLACEMENT BASED FORMULATION FOR MORTAR/INTERFACE ELEMENTS

A limitation of the traditional interface element is that upper and lower faces have to match each other, that is, that nodes 1 and 3 in Figure 1, as well as nodes 2 and 4, have to coincide or face each other perfectly. That means that meshes on

both sides of the discontinuity have to match each other perfectly at that line. This requirement also limits the extent of the analysis in the sense that interface opening and (especially) sliding have to be limited to values sufficiently small with respect to the original interface element length, so that the original node pairing is sensibly maintained. The developments in the present section set the basis for overcoming those limitations, with the formulation of the mortar/interface element in which nodes (and meshes on both sides) do not need to match each other.

3.1 | Mortar/interface element geometry, local coordinates and interpolation

The basic geometry and definitions of the zero-thickness mortar/interface element are represented in Figure 2.

The surfaces in contact are denoted as "surface A" (bottom side in the figure) and "surface "B" (top side). The mortar/interface contact surface (or "surface C" in the figure) is defined, in general terms, as the line at mid-distance in between the two contact sides. Although this concept may be not totally unambiguous in the contact between irregular surfaces, for the sake of simplicity and with the purpose of developing the FE formulation, attention here is restricted to cases in which the mid-distance surface is well defined, and all other cases are left out for future consideration. The discretization into mortar/interface elements is achieved by projecting all the nodes from each side onto the midplane mortar interface surface (for instance by using the normal to the midplane surface itself), and then defining one mortar element for each one of the resulting segments. In this way, each mortar segment, denoted from now on as mortar/interface element, will overlap a single element face on each side of the discontinuity or contact, as represented in Figure 2. This definition has been already used in existing literature[21,31–33] and has the advantage of totally symmetric treatment of the two contact surfaces (and avoiding the otherwise necessary choice between master and slave surfaces, which may be in many cases totally arbitrary). A standard displacement-based interpolation is defined independently for each the two sides of the mortar-interface element, as well as for the mortar segment itself, as represented in Figure 3.

For the element face of surface A, interpolation is based on shape functions $N_A^{(i)}(\xi_A)$, where ξ_A is the classical local coordinate varying in the range $[-1, 1]$ along the "A" element surface, and $i = 1, 2$ is the end-node index of the corresponding element face. Similarly, local coordinate ξ_B and shape functions $N_B^{(i)}(\xi_B)$ are considered for the element face of Surface B. Additional to the local coordinates on both contact sides A and B, a third local coordinate ξ_C also varying in the range $[-1, 1]$ is defined along the midplane surface of the interface/mortar element segment, as well as the corresponding interpolation functions $N_C^{(i)}(\xi_C)$.

Along this midplane "C" surface is precisely where the element integrations will be performed to obtain stiffness matrices, etc. and for this purpose, a correspondence has to be established between the mortar local coordinate ξ_C and the contact surface coordinates ξ_A, ξ_B. This is achieved by using the same mortar interpolation functions $N_C^{(i)}(\xi_C)$,

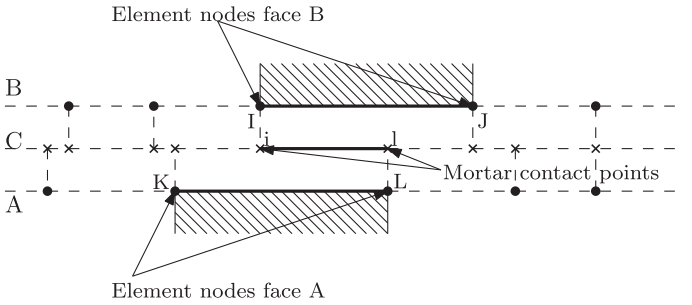

FIGURE 2 Geometry of the mortar/interface element (central line), and element faces on each side of interface or contact

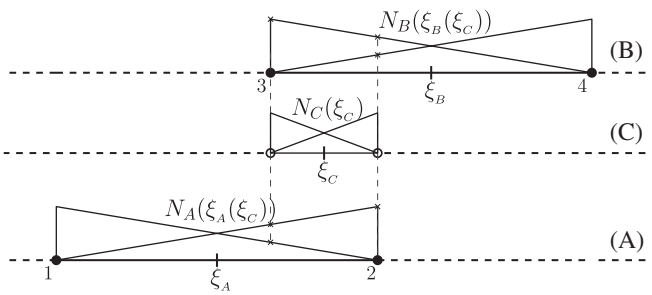

FIGURE 3 Geometry of standard mortar interface element

that is:

$$\xi_A(\xi_C) = \sum_{i=1}^{2} N_C^{(i)}(\xi_C)\, \xi_A^{(i)}$$
$$\xi_B(\xi_C) = \sum_{i=1}^{2} N_C^{(i)}(\xi_C)\, \xi_B^{(i)}, \tag{15}$$

where $\xi_A^{(i)}$ and $\xi_B^{(i)}$ are the local coordinates on surfaces A and B of the end points of the mortar segment on surface C (i.e., projection of the point with $\xi_C = -1$ for i =1, and of the point with $\xi_C = +1$ for $i = 2$).

3.2 | Relative displacements and contact stresses

The absolute displacement $\boldsymbol{u_A}$ of any point on the contact surface A of the mortar/interface element is assumed to be provided by standard interpolation along that surface using shape functions $N_A^{(i)}(\xi_A)$ and similarly, for the absolute displacement $\boldsymbol{u_B}$ on the contact surface B:

$$\boldsymbol{u_A}(\xi_A) = \sum_{i=1}^{2} N_A^{(i)}(\xi_A)\boldsymbol{u}_A^{(i)} \qquad \text{or} \qquad \boldsymbol{u_A}(\xi_A) = \mathbf{N}_A(\xi_A)\, \boldsymbol{u}_A^{el},$$
$$\boldsymbol{u_B}(\xi_B) = \sum_{i=1}^{2} N_B^{(i)}(\xi_B)\boldsymbol{u}_B^{(i)} \qquad \text{or} \qquad \boldsymbol{u_B}(\xi_B) = \mathbf{N}_B(\xi_B)\, \boldsymbol{u}_B^{el}, \tag{16}$$

where $\boldsymbol{u}_A^{(i)}$ are the nodal displacement values on surface A (end points of the element face with local coordinates $\xi_A = -1$ for i =1, and with $\xi_A = +1$ for $i = 2$), which may be collected in a single vector $\boldsymbol{u}_A^{el}$ and, similarly, $\boldsymbol{u}_B^{(i)}$ are the nodal displacement values at the ends of surface B, which can be collected in the single vector $\boldsymbol{u}_B^{el}$. All these nodal values are also collected in the single overall displacement vector of the mortar/interface element $\boldsymbol{u}^{el}$. The interpolation matrices have the structure

$$\mathbf{N}_A(\xi_A) = \left[\mathbf{N}_A^{(1)}(\xi_A) \;\middle|\; \mathbf{N}_A^{(2)}(\xi_A)\right], \mathbf{N}_B(\xi_B) = \left[\mathbf{N}_B^{(1)}(\xi_B) \;\middle|\; \mathbf{N}_B^{(2)}(\xi_B)\right], \tag{17}$$

where

$$\mathbf{N}_A^{(1)}(\xi_A) = N_A^{(1)}(\xi_A)\, \mathbf{I}, \quad \mathbf{N}_A^{(2)}(\xi_A) = N_A^{(2)}(\xi_A)\, \mathbf{I}, \quad \mathbf{N}_B^{(1)}(\xi_B) = N_B^{(1)}(\xi_B)\, \mathbf{I}, \quad \mathbf{N}_B^{(2)}(\xi_B) = N_B^{(2)}(\xi_B)\, \mathbf{I}. \tag{18}$$

Relative displacements in global x,y axes, $\boldsymbol{r}^{xy}$, at a point of the mortar/interface element, defined by a local coordinate ξ_C, are obtained as the difference between the absolute displacements of the corresponding projection points on A and B defined by mapping equations $\xi_A(\xi_C)$ and $\xi_B(\xi_C)$ above (15), that is:

$$\boldsymbol{r}^{xy}(\xi_C) = \boldsymbol{u_B}(\xi_B(\xi_C)) - \boldsymbol{u_A}(\xi_A(\xi_C)) = \mathbf{N}_B(\xi_B(\xi_C))\boldsymbol{u}_B^{el} - \mathbf{N}_A(\xi_A(\xi_C))\boldsymbol{u}_A^{el} = \mathbf{N}_{el}(\xi_C)\, \boldsymbol{u}^{el}, \tag{19}$$

where the element interpolation matrix $\mathbf{N}^{el}$ has the structure:

$$\mathbf{N}^{el}(\xi_C) = [-\mathbf{N}_A(\xi_A(\xi_C))|\, \mathbf{N}_B(\xi_B(\xi_C))] = \left[-\mathbf{N}_A^{(1)}(\xi_A(\xi_C))\right| \left.-\mathbf{N}_A^{(2)}(\xi_A(\xi_C))\right| \left.\mathbf{N}_B^{(1)}(\xi_B(\xi_C))\right| \left.\mathbf{N}_B^{(2)}(\xi_B(\xi_C))\right]. \tag{20}$$

Note that arguments of the shape functions have been made explicit to emphasize parametrization in terms of the mortar local coordinate ξ_C. Relative displacements in global x,y axes are then rotated to local axes n,t, by means of local rotation matrix $\mathbf{R}$:

$$\boldsymbol{r}(\xi_C) = \mathbf{R}\, \boldsymbol{r}^{xy}(\xi_C) = \mathbf{R}\, \mathbf{N}^{el}(\xi_C)\, \boldsymbol{u}^{el} = \mathbf{B}^{el}(\xi_c)\, \boldsymbol{u}^{el}, \tag{21}$$

where parametrization in terms of the mortar local coordinate ξ_c has also been emphasized. Note that the overall "B" matrix of the element $\mathbf{B}^{el}$, has the structure

$$\mathbf{B}^{el}(\xi_c) = [\mathbf{B}_A(\xi_A(\xi_C))|\, \mathbf{B}_B(\xi_B(\xi_C))] = \left[\mathbf{B}_A^{(1)}(\xi_A(\xi_C)) \;\middle|\; \mathbf{B}_A^{(2)}(\xi_A(\xi_C))\middle|\; \mathbf{B}_B^{(1)}(\xi_B(\xi_C))\middle|\; \mathbf{B}_B^{(2)}(\xi_B(\xi_C))\right], \tag{22}$$

where

$$\mathbf{B}_A^{(1)}(\xi_A(\xi_C)) = -\mathbf{R}\,\mathbf{N}_A^{(1)}(\xi_A(\xi_C)),\;\; \mathbf{B}_A^{(2)}(\xi_A) = -\mathbf{R}\,\mathbf{N}_A^{(2)}(\xi_A(\xi_C)),\;\; \mathbf{B}_B^{(1)}(\xi_B) = \mathbf{R}\,\mathbf{N}_B^{(1)}(\xi_B),\;\; \mathbf{B}_B^{(2)}(\xi_B) = \mathbf{R}\,\mathbf{N}_B^{(2)}(\xi_B). \tag{23}$$

Same as for the traditional interface model, relative displacements (21) are replaced into the general format of linear constitutive equation (5), which leads to the stress traction at a point of the mortar interface:

$$\boldsymbol{t} = \boldsymbol{D}\mathbf{B}^{el}(\xi_c)\,\boldsymbol{u}^{el} + \boldsymbol{t}_0. \tag{24}$$

3.3 | Application of the PVW and derivation of element stiffness matrix

Once the expressions of the relative displacements (21) and stress tractions (24) have been obtained, the stiffness matrix displacement-formulation of the mortar element is derived by standard application of the PVW, with expressions identical to the ones obtained for the traditional interface element (8)–(10). However, due to the particular structure of the "B" matrix involved, the stiffness matrix may be also decomposed into four submatrices

$$\mathbf{K}^{el} = \int_{S_c} \begin{bmatrix}(\mathbf{B}_A)^T\\(\mathbf{B}_B)^T\end{bmatrix} \boldsymbol{D}[\,\mathbf{B}_A|\,\mathbf{B}_B]\; dS_C = \int_{S_c} \begin{bmatrix}(\mathbf{B}_A)^T\boldsymbol{D}\mathbf{B}_A & (\mathbf{B}_A)^T\boldsymbol{D}\mathbf{B}_B\\(\mathbf{B}_B)^T\boldsymbol{D}\mathbf{B}_A & (\mathbf{B}_B)^{\mathrm{T}}\mathbf{D}\mathbf{B}_B\end{bmatrix}\; dS_C = \begin{bmatrix}\mathbf{k}_{AA} & \mathbf{k}_{AB}\\\mathbf{k}_{BA} & \mathbf{k}_{BB}\end{bmatrix}, \tag{25}$$

where

$$\mathbf{k}_{AA} = \int_{S_c} (\mathbf{B}_A)^T\boldsymbol{D}\mathbf{B}_A dS_C, \quad \mathbf{k}_{AB} = \int_{S_c} (\mathbf{B}_A)^T\boldsymbol{D}\mathbf{B}_B dS_C, \quad \mathbf{k}_{BA} = \int_{S_c} (\mathbf{B}_B)^T\boldsymbol{D}\mathbf{B}_A dS_C, \quad \mathbf{k}_{BB} = \int_{S_c} (\mathbf{B}_B)^T\boldsymbol{D}\mathbf{B}_B dS_C. \tag{26}$$

A similar structure can be found for the initial force vector

$$\boldsymbol{F}_0^{el} = \begin{bmatrix}\boldsymbol{f}_{A0}\\\boldsymbol{f}_{B0}\end{bmatrix}, \qquad \boldsymbol{f}_{A0} = \int_{S_c} (\mathbf{B}_A)^T\boldsymbol{t}_0 dS_C, \qquad \boldsymbol{f}_{B0} = \int_{S_c} (\mathbf{B}_B)^T\boldsymbol{t}_0 dS_C. \tag{27}$$

3.4 | Comparison to traditional zero-thickness interface elements

The expressions obtained for the mortar element (25)–(27), may be compared with those obtained in Section 2 for the traditional interface element (9)–(13). By doing so, one finds that, if surfaces A and B match each other (and therefore also C), local coordinates also coincide and B matrices take the values:

$$\begin{gathered}\xi_A = \xi_B = \xi_C = \xi\\ \mathbf{B}_A(\xi) = [\;\mathbf{B}_1(\xi)\;|\;\mathbf{B}_2(\xi)], \qquad \mathbf{B}_B(\xi) = [\,\mathbf{B}_3(\xi)|\;\mathbf{B}_4(\xi)\;],\end{gathered} \tag{28}$$

which leads to equivalent vectors and matrices in both cases:

$$\begin{gathered}\mathbf{k}_{AA} = -\mathbf{k}_{AB} = -\mathbf{k}_{BA} = \mathbf{k}_{BB} = \mathbf{k}_{MP},\\ \boldsymbol{f}_{A0} = \boldsymbol{f}_{B0} = \boldsymbol{f}_0^{el}.\end{gathered} \tag{28bis}$$

That is, in the case that surfaces A and B match each other, the mortar element collapses into a traditional zero-thickness interface element, and the stiffness matrix and initial force vector of both displacement-based formulations coincide.

4 | HYBRID FORMULATION FOR MORTAR/INTERFACE ELEMENTS

4.1 | Introduction

The displacement-based formulation developed in Section 3 is well suited for cases in which the constitutive behavior of the discontinuity (interface, contact, or crack), represented by the mortar/interface element, may be described via relative displacement ("strain")-driven constitutive model with an always well-defined incremental (tangential) stiffness matrix. This is the case for instance if the model is elastoplastic (perfect plasticity or hardening/softening), as it has been traditionally used for small-strain (in fact small relative displacement) behavior of existing discontinuities or developing cracks in the geotechnical or structural context.[27,28] However, sometimes it may be more advantageous to use a stress-driven constitutive description, such as for instance viscoplasticity, in which tangential compliance matrix is the primer definition (rather than stiffness matrix). That case and also the simple study of alternative formats of the finite element formulation, motivate the development of the hybrid formulation of the mortar/interface element in the following subsections.

4.2 | Basic interpolation in terms of stress tractions

In the hybrid formulation, the main interpolation along the mortar surface C itself, is established in terms of stress tractions in x,y axes, $\boldsymbol{t}^{xy}$, rather than relative displacements. This interpolation may be expressed as follows:

$$\boldsymbol{t}^{xy}(\xi_C) = \sum_{i=1}^{2} \overline{N}_C^{(i)}(\xi_C)\, \boldsymbol{t}^{(i)} \qquad \text{or} \qquad \boldsymbol{t}^{xy}(\xi_C) = \overline{\mathbf{N}}_C(\xi_C)\, \widehat{\boldsymbol{t}}^{el}, \tag{29}$$

where $\boldsymbol{t}^{(i)}$ are the nodal traction vectors in x,y components, at nodes (i) of the mortar surface segment C (in the linear version presented here, the two nodes corresponding to the left and right end points α and β located at $\xi_C = -1$, and $\xi_C = +1$, respectively), which may be collected in a single "reduced" element force vector, $\widehat{\boldsymbol{t}}^{el}$. The interpolation matrix has the structure

$$\overline{\mathbf{N}}_C(\xi_C) = \left[\, \overline{\mathbf{N}}_C^{(1)}(\xi_C) \;\middle|\; \overline{\mathbf{N}}_C^{(2)}(\xi_C) \right] \text{wherein } \overline{\mathbf{N}}_C^{(1)}(\xi_C) = \overline{N}_C^{(1)}(\xi_C)\, \mathbf{I}, \quad \overline{\mathbf{N}}_C^{(2)}(\xi_C) = \overline{N}_C^{(2)}(\xi_C)\, \mathbf{I}. \tag{30}$$

Stress tractions in global x,y axes are then rotated to local axes n,t, by means of local rotation matrix $\mathbf{R}$:

$$\boldsymbol{t}(\xi_C) = \mathbf{R}\, \boldsymbol{t}^{xy}(\xi_C) = \mathbf{R}\, \overline{\mathbf{N}}_C(\xi_C)\, \widehat{\boldsymbol{t}}^{el} = \overline{\mathbf{B}}_C(\xi_C)\, \widehat{\boldsymbol{t}}^{el}, \tag{31}$$

where parametrization in terms of the mortar local coordinate ξ_c has also been emphasized. Note that the mortar "B" matrix of the element $\overline{\mathbf{B}}_C(\xi_c)$ has the structure

$$\overline{\mathbf{B}}_C(\xi_c) = \left[\overline{\mathbf{B}}_C^{(1)}(\xi_C) \;\middle|\; \overline{\mathbf{B}}_C^{(2)}(\xi_C) \right], \tag{32}$$

where

$$\overline{\mathbf{B}}_C^{(1)}(\xi_C) = \mathbf{R}\, \overline{\mathbf{N}}_C^{(1)}(\xi_C), \qquad \overline{\mathbf{B}}_C^{(2)}(\xi_C) = \mathbf{R}\, \overline{\mathbf{N}}_C^{(2)}(\xi_C). \tag{33}$$

According to the general philosophy of hybrid elements,[34] the above interpolation of the stresses inside the element (traction field along the mortar surface C) coexists with the interpolation of displacements along the element boundaries (both side surfaces A and B), as defined by Equations (16)–(18). All previous definitions are illustrated in Figure 4.

In order to develop the element formulation of the hybrid matrix/interface element, the principle of virtual work will be applied twice. First, in the form of principle of complementary virtual work (PCVW) along the mortar surface C itself (Section 4.3), and then in the direct form of PVW along the contact of mortar surface C and side surfaces A and B (Section 4.4).

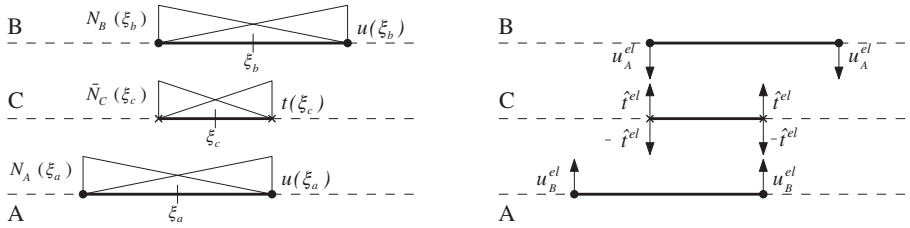

(A) Shape functions (B) Variables interpolated

FIGURE 4 Basic stress-displacement interpolation

4.3 | Application of the PCVW along surface C, reduced compliance and stiffness matrices

The PCVW is applied between stress tractions $\boldsymbol{t}(\xi_c)$ and relative displacements $\boldsymbol{r}(\xi_c)$ along the mortar surface C, leading to the following expression:

$$(\delta\hat{\boldsymbol{t}}^{el})^T\,\hat{\boldsymbol{r}}^{el} = \int_{S_c} (\delta\boldsymbol{t}(\xi_C))^T \boldsymbol{r}(\xi_C) dS_C, \tag{34}$$

where δ represents a virtual variation, and $\hat{\boldsymbol{r}}^{el}$ is the vector of relative nodal displacement values in *x,y* coordinates for the mortar segment C, which is the conjugate pair to the vector of nodal traction values for the same segment, $\hat{\boldsymbol{t}}^{el}$. Vector $\hat{\boldsymbol{r}}^{el}$ is a necessary ingredient of a hybrid formulation, which in this case has the clear physical meaning of the *x,y* relative displacements at the two ends of the mortar segment. By introducing the stress traction interpolation (29) in the right-hand side of (34), it is possible to eliminate the virtual variation $\delta\hat{\boldsymbol{t}}^{el}$ on both sides of the equation to finally obtain:

$$\hat{\boldsymbol{r}}^{el} = \int_{S_c} \overline{\mathbf{B}}_C^{\,T}(\xi_c)\, \boldsymbol{r}(\xi_C)\, dS_C, \tag{35}$$

which constitutes the weak form of compatibility, dual to the standard weak equilibrium equation in displacement-based formulations (8).

In the hybrid formulation, the general form of linear constitutive behavior of a point on the mortar discontinuity surface (5) is more advantageously introduced in terms of compliance as:

$$\boldsymbol{r} = \boldsymbol{C}\,\boldsymbol{t} + \boldsymbol{r}_0, \tag{36}$$

where $\boldsymbol{C} = \boldsymbol{D}^{-1}$ is the constitutive compliance matrix, and $\boldsymbol{r}_0 = -\boldsymbol{C}\,\boldsymbol{t}_0$ is the initial relative displacement vector. If $\boldsymbol{r}$ from (36) is introduced in (35), and then $\boldsymbol{t}$ is replaced with the interpolation expression (31), one obtains:

$$\hat{\boldsymbol{r}}^{el} = \hat{\mathbf{C}}^{el}\,\hat{\boldsymbol{t}}^{el} + \hat{\boldsymbol{r}}_0^{el}, \tag{37}$$

where $\hat{\mathbf{C}}^{el}$ and $\hat{\boldsymbol{r}}_0^{el}$ are the "reduced" compliance matrix and the "reduced" initial relative displacement vector, with expressions:

$$\begin{aligned} \hat{\mathbf{C}}^{el} &= \int_{S_c} \overline{\mathbf{B}}_C^{\,T}(\xi_c)\boldsymbol{D}^{-1}\,\overline{\mathbf{B}}_C(\xi_c) dS_C, \\ \hat{\boldsymbol{r}}_0^{el} &= \int_{S_c} \overline{\mathbf{B}}_C^{\,T}(\xi_c)\boldsymbol{r}_0(\xi_c)\, dS_C. \end{aligned} \tag{38}$$

Finally, relation (37) can be inverted to obtain

$$\hat{\boldsymbol{t}}^{el} = \hat{\mathbf{D}}^{el}\,\hat{\boldsymbol{r}}^{el} - \hat{\boldsymbol{t}}_0^{el}, \tag{39}$$

where the "reduced" stiffness matrix and "reduced" initial force vector have expressions:

$$\begin{aligned}\widehat{\mathbf{D}}^{el} &= (\widehat{\mathbf{C}}^{el})^{-1},\\ \widehat{\boldsymbol{t}}_0^{el} &= -\widehat{\mathbf{D}}^{el}\,\widehat{\boldsymbol{r}}_0^{el}.\end{aligned} \tag{40}$$

4.4 | Application of the PVW between surfaces A and C, and B and C

The matrix equations of the previous section relate the "reduced" force and the "reduced" relative displacement vectors, $\widehat{\boldsymbol{t}}^{el}$ and $\widehat{\boldsymbol{r}}^{el}$. To obtain the general matrix relation between standard force and displacement vectors of the element, $\boldsymbol{F}^{el}$ and $\boldsymbol{u}^{el}$, the latter has to be related to the former. In order to do that, it is convenient first to define vector $\boldsymbol{t}_{CA}^{xy}$ of stress tractions applied at any point of AC (part of surface A overlapping with mortar surface C), and similarly vector $\boldsymbol{t}_{CB}^{xy}$ of the stress tractions applied at any point of BC (part of surface B overlapping with mortar surface C). Those traction vectors have the same magnitude and opposite directions, and have to be equal in magnitude to the stress traction $\boldsymbol{t}^{xy}$at the same point along the mortar surface C:

$$\begin{aligned}\boldsymbol{t}_{CA}^{xy}(\xi_C) &= \boldsymbol{t}^{xy}(\xi_C),\\ \boldsymbol{t}_{CB}^{xy}(\xi_C) &= -\boldsymbol{t}^{xy}(\xi_C).\end{aligned} \tag{41}$$

The PVW is then applied along AC, between the stress tractions $\boldsymbol{t}_{CA}^{xy}$ and the displacements taking place over that surface $\boldsymbol{u}_A$, which have to be equal to the corresponding virtual work at nodes of side surface A:

$$(\delta\boldsymbol{u}_A^{el})^T\boldsymbol{F}_A = \int_{S_c}(\delta\boldsymbol{u}_A(\xi_A(\xi_C)))^T\boldsymbol{t}_{CA}^{xy}(\xi_C)\;\,dS_C, \tag{42}$$

where $\boldsymbol{F}_A$ are the nodal forces on surface A. Combining this expression with (41) and with the interpolations of stress tractions and displacements, Equations (29) and (16), and enforcing the resulting equation for any virtual variation of displacements $\delta\boldsymbol{u}_A^{el}$, the following expression is obtained:

$$\boldsymbol{F}_A = \mathbf{T}_{AC}\,\widehat{\boldsymbol{t}}^{el}, \tag{43}$$

where $\mathbf{T}_{AC}$ is the "transfer" matrix relating the forces applied on element side A and on mortar surface C, with expression:

$$\mathbf{T}_{AC} = \int_{S_c}\mathbf{N}_A{}^T(\xi_A(\xi_C))\,\overline{\mathbf{N}}_C(\xi_C)\,dS_C. \tag{44}$$

Similar application of the PVW along surface BC, leads to the similar relation:

$$\boldsymbol{F}_B = -\mathbf{T}_{BC}\,\widehat{\boldsymbol{t}}^{el}, \tag{45}$$

where the transfer matrix between side B and mortar surface C is defined as

$$\mathbf{T}_{BC} = \int_{S_c}\mathbf{N}_B{}^T(\xi_B(\xi_C))\overline{\mathbf{N}}_C(\xi_C)\,dS_C. \tag{46}$$

4.5 | Dual kinematic relations

To obtain the final hybrid mortar element formulation, additional relations between $\widehat{\boldsymbol{r}}^{el}$ and $\boldsymbol{u}_A$, $\boldsymbol{u}_B$, dual to (43) and (45), are also required. For this purpose, the absolute displacements of both sides of the mortar surface at a point ξ_C of that surface, $\boldsymbol{u}_{CA}^{xy}(\xi_C)$ and $\boldsymbol{u}_{CB}^{xy}(\xi_C)$ are introduced, which by definition satisfy:

$$\boldsymbol{u}_{CB}^{xy}(\xi_C) - \boldsymbol{u}_{CA}^{xy}(\xi_C) = \widehat{\boldsymbol{r}}^{el}(\xi_C). \tag{47}$$

Note, however, that in contrast to the assumption made for stresses (41), in this formulation the mortar displacements $\boldsymbol{u}_{CA}^{xy}(\xi_C)$ and $\boldsymbol{u}_{CB}^{xy}(\xi_C)$ will not generally coincide with the displacements of the corresponding points on surfaces A and B, $\boldsymbol{u}_A(\xi_A(\xi_C))$ and $\boldsymbol{u}_B(\xi_B(\xi_C))$ and, for this reason, the missing relations have to be established in a weak sense. This may be accomplished by taking advantage of relations (43) and (45) and applying again of the PCVW between the nodal forces and displacements on element sides A and B, and the "reduced" vectors of stress tractions $\widehat{\boldsymbol{t}}^{el}$ and nodal displacements $\widehat{\boldsymbol{r}}^{el}$ on the mortar surface C. As the result, one may obtain:

$$(\delta\widehat{\boldsymbol{t}}^{el})^T\widehat{\boldsymbol{r}}^{el} = (\delta\boldsymbol{F}_A)^T\boldsymbol{u}_A^{el} + (\delta\boldsymbol{F}_B)^T\boldsymbol{u}_B^{el}. \tag{48}$$

Replacing now $\delta\boldsymbol{F}_A$, $\delta\boldsymbol{F}_B$with (43) and (45), and enforcing that the resulting expression be satisfied for any value of $\delta\widehat{\boldsymbol{t}}^{el}$, one finally obtains:

$$\widehat{\boldsymbol{r}}^{el} = (\mathbf{T}_{AC})^T\,\boldsymbol{u}_A^{el} - (\mathbf{T}_{BC})^T\boldsymbol{u}_B^{el}. \tag{49}$$

4.6 | Final stiffness matrix and force vector for the hybrid formulation of the mortar/interface elements

Combining the Equations (39) and (49) and introducing in expression (43) one can obtain:

$$\boldsymbol{F}_A = \mathbf{T}_{AC}(\widehat{\mathbf{C}}^{el})^{-1}(\mathbf{T}_{AC})^T\,\boldsymbol{u}_A^{el} - \mathbf{T}_{AC}(\widehat{\mathbf{C}}^{el})^{-1}(\mathbf{T}_{BC})^T\boldsymbol{u}_B^{el} - \mathbf{T}_{AC}\widehat{\boldsymbol{t}}_0^{el}. \tag{50}$$

Equally, the same equations may be replaced into (45) to obtain:

$$\boldsymbol{F}_B = -\mathbf{T}_{BC}(\widehat{\mathbf{C}}^{el})^{-1}(\mathbf{T}_{AC})^T\,\boldsymbol{u}_A^{el} + \mathbf{T}_{BC}(\widehat{\mathbf{C}}^{el})^{-1}(\mathbf{T}_{BC})^T\boldsymbol{u}_B^{el} + \mathbf{T}_{BC}\widehat{\boldsymbol{t}}_0^{el}. \tag{51}$$

The two previous equations may be collected and reordered in matrix form, which constitutes the final matrix equation for the hybrid mortar-interface element:

$$\boldsymbol{F}^{el} = \mathbf{K}^{el}\,\boldsymbol{u}^{el} + \boldsymbol{F}_0^{el}. \tag{52}$$

$$\mathbf{K}^{el} = \begin{bmatrix} \mathbf{T}_{AC}(\hat{\mathbf{C}}^{el})^{-1}\mathbf{T}_{AC}{}^T & -\mathbf{T}_{AC}(\hat{\mathbf{C}}^{el})^{-1}\mathbf{T}_{BC}{}^T \\ -\mathbf{T}_{BC}(\hat{\mathbf{C}}^{el})^{-1}\mathbf{T}_{AC}{}^T & \mathbf{T}_{BC}(\hat{\mathbf{C}}^{el})^{-1}\mathbf{T}_{BC}{}^T \end{bmatrix}, \qquad \boldsymbol{F}_0^{el} = \begin{vmatrix} -\mathbf{T}_{AC}\hat{\boldsymbol{t}}_0^{el} \\ \mathbf{T}_{BC}\hat{\boldsymbol{t}}_0^{el} \end{vmatrix} \tag{53}$$

or:

$$\mathbf{K}^{el} = \begin{vmatrix} -\mathbf{T}_{AC} \\ \mathbf{T}_{BC} \end{vmatrix} (\widehat{\mathbf{C}}^{el})^{-1}[\,-\mathbf{T}_{AC}{}^T \;\vert\; \mathbf{T}_{BC}{}^T\,], \qquad \boldsymbol{F}_0^{el} = \begin{vmatrix} -\mathbf{T}_{AC} \\ \mathbf{T}_{BC} \end{vmatrix} \widehat{\boldsymbol{t}}_0^{el}. \tag{53bis}$$

4.7 | Special case of matching nodes: Hybrid formulation of zero-thickness interface elements

It is of interest to specify the general hybrid mortar interface equations obtained in the previous section, to the special case in which surfaces A and B match each other, and therefore geometrically speaking the mortar element collapses into a traditional interface element.

If surfaces A, B, and C match each other, the corresponding local coordinates coincide. Thus, shape functions, interpolation matrices and "B" matrices, for surfaces A and B also coincide, that is:

$$\begin{gathered} \xi_A = \xi_B = \xi_C = \xi \\ N_A^{(i)}(\xi_A) = N_B^{(i)}(\xi_B) = N^{(i)}(\xi), \qquad \mathbf{N}_A(\xi_A) = \mathbf{N}_B(\xi_B) = \mathbf{N}(\xi) \\ \mathbf{B}_A(\xi_A) = \mathbf{B}_B(\xi_B) = \mathbf{B}(\xi) = \mathbf{R}\,\mathbf{N}(\xi). \end{gathered} \tag{54}$$

Shape functions, interpolation matrices and B matrices for surface C are also assumed to be the same as for A, B:

$$\begin{aligned} \overline{N}_C^{(i)}(\xi_C) = N^{(i)}(\xi), \;\; \overline{\mathbf{N}}_C(\xi_C) = \mathbf{N}(\xi), \\ \overline{\mathbf{B}}_C(\xi_C) = \mathbf{B}(\xi) = \mathbf{R}\mathbf{N}(\xi). \end{aligned} \tag{55}$$

With those specifications, the reduced compliance and initial relative displacement vectors become:

$$\begin{aligned} \widehat{\mathbf{C}}^{el} = \int_{S_c} \mathbf{B}^T(\xi) \boldsymbol{D}^{-1} \, \mathbf{B}(\xi) dS_C, \\ \widehat{\boldsymbol{r}}_0^{el} = \int_{S_c} \mathbf{B}^T(\xi) \boldsymbol{r}_0(\xi) \, dS_C \end{aligned} \tag{56}$$

and transfer matrices read:

$$\mathbf{T}_{AC} = \mathbf{T}_{BC} = \mathbf{T} = \int_{S_c} \mathbf{N}^T(\xi) \;\; \mathbf{N}(\xi) \, dS_C. \tag{57}$$

The final stiffness matrix and initial force vector, become:

$$\mathbf{K}^{el} = \begin{vmatrix} -\mathbf{T} \\ \mathbf{T} \end{vmatrix} (\widehat{\mathbf{C}}^{el})^{-1} [\, -\mathbf{T}^T \;\; | \;\; \mathbf{T}^T \;\;], \qquad \boldsymbol{F}_0^{el} = \begin{vmatrix} -\mathbf{T} \\ \mathbf{T} \end{vmatrix} \widehat{\boldsymbol{t}}_0^{el}, \tag{58}$$

in which $\widehat{\boldsymbol{t}}_0^{el}$ is obtained using (40b). The above equation may be alternatively rewritten as:

$$\mathbf{K}^{el} = \begin{vmatrix} -\mathbf{I}_4 \\ \mathbf{I}_4 \end{vmatrix} \widehat{\mathbf{k}}^{el} [\, -\mathbf{I}_4 \;\; | \;\; \mathbf{I}_4 \;\;], \qquad \boldsymbol{F}_0^{el} = \begin{vmatrix} -\mathbf{I}_4 \\ \mathbf{I}_4 \end{vmatrix} \widehat{\boldsymbol{f}}_0^{el}, \tag{59}$$

where:

$$\widehat{\mathbf{k}}^{el} = \mathbf{T} \, (\widehat{\mathbf{C}}^{el})^{-1} \mathbf{T}^T, \qquad \widehat{\boldsymbol{f}}_0^{el} = \mathbf{T} \, \widehat{\boldsymbol{t}}_0^{el}. \tag{60}$$

The above Equations (56-60) constitute a new alternative formulation of the hybrid type for the traditional zero-thickness interface element.

5 | EQUIVALENCE BETWEEN DISPLACEMENT-BASED AND HYBRID FORMULATIONS FOR MATCHING NODES, LINEAR ELASTICITY, AND CONSTANT STIFFNESS

Comparing the stiffness matrix of the classical displacement-based formulation of the standard zero-thickness interface element (12, 13) with the corresponding expressions for the hybrid formulation described above (59, 60), the structure is similar, with four quadrants consisting of a submatrix repeated four times with alternate signs. This submatrix, $\mathbf{k}_{MP}$ in the displacement-based formulation and $\widehat{\mathbf{k}}^{el}$ in the hybrid formulation, represent the intrinsic stiffness of the interface element in terms of relative displacements and pairs of forces on the interface midplane or mortar surface. In the general case of nonconstant stiffness (either because of linear elasticity with nonconstant properties, or because of nonlinear constitutive behavior and variable stress state along the interface surface), matrices $\mathbf{k}_{MP}$ and $\widehat{\mathbf{k}}^{el}$ are not equivalent. However, in the special case of constant stiffness along the interface, the two matrices may be shown to be identical, as developed in subsequent paragraphs.

To show this equivalence, Equations (11) and (2) are replaced in the expression of the intrinsic compliance matrix of the hybrid element (56a), the interpolation functions along the mortar surface are assumed equivalent and the constitutive

stiffness matrix in *x,y* components, $\boldsymbol{D}^{xy}$, is identified and replaced:

$$\hat{\mathbf{C}}^{el} = \int_{S_c} \begin{vmatrix} N^{(\alpha)}(\xi)\,\mathbf{I} \\ N^{(\beta)}(\xi)\,\mathbf{I} \end{vmatrix} (\boldsymbol{D}^{xy})^{-1} \left[N^{(\alpha)}(\xi)\,\mathbf{I} \,\middle|\, N^{(\beta)}(\xi)\,\mathbf{I} \right] dS_C, \qquad \boldsymbol{D}^{\mathrm{xy}} = \mathbf{R}^{\mathrm{T}} \boldsymbol{D}\, \mathbf{R}. \tag{61}$$

By developing the vector products and introducing the integrals in the matrix components, the expression becomes

$$\hat{\mathbf{C}}^{el} = \begin{bmatrix} \mathcal{J}_{\alpha\alpha}(\boldsymbol{D}^{\boldsymbol{xy}})^{-1} & \mathcal{J}_{\alpha\beta}(\boldsymbol{D}^{\boldsymbol{xy}})^{-1} \\ \mathcal{J}_{\alpha\beta}(\boldsymbol{D}^{\boldsymbol{xy}})^{-1} & \mathcal{J}_{\beta\beta}(\boldsymbol{D}^{\boldsymbol{xy}})^{-1} \end{bmatrix}, \tag{62}$$

where $\mathcal{J}_{\alpha\alpha}, \mathcal{J}_{\alpha\beta}, \mathcal{J}_{\beta\beta}$ are the integrals:

$$\mathcal{J}_{\alpha\alpha} = \int_{S_C} (N^{(\alpha)})^2 dS_C, \qquad \mathcal{J}_{\beta\beta} = \int_{S_C} (N^{(\beta)})^2 dS_C, \qquad \mathcal{J}_{\alpha\beta} = \int_{S_C} N^{(\alpha)} N^{(\beta)} dS_C. \tag{63}$$

Expression (62) may be inverted to obtain:

$$(\hat{\mathbf{C}}^{el})^{-1} = \frac{1}{\mathcal{J}_{\alpha\alpha}\,\mathcal{J}_{\beta\beta} - (\mathcal{J}_{\alpha\beta})^2} \begin{bmatrix} \mathcal{J}_{\beta\beta}\,\boldsymbol{D}^{xy} & -\mathcal{J}_{\alpha\beta}\,\boldsymbol{D}^{xy} \\ -\mathcal{J}_{\alpha\beta}\,\boldsymbol{D}^{xy} & \mathcal{J}_{\alpha\alpha}\,\boldsymbol{D}^{xy} \end{bmatrix}. \tag{64}$$

Matrix **T** (57) needs also to be evaluated. If (2) is replaced in (57) the matrix product is developed and the integral is introduced in the components of the matrix, one obtains:

$$\mathbf{T} = \begin{bmatrix} \mathcal{J}_{\alpha\alpha}\,\mathbf{I} & \mathcal{J}_{\alpha\beta}\,\mathbf{I} \\ \mathcal{J}_{\alpha\beta}\,\mathbf{I} & \mathcal{J}_{\beta\beta}\,\mathbf{I} \end{bmatrix} \tag{65}$$

and then, introducing this and (64) into (60), leads to the final expression of the intrinsic stiffness for the hybrid formulation:

$$\hat{\mathbf{k}}^{el} = \mathbf{T}\,(\hat{\mathbf{C}}^{el})^{-1}\mathbf{T}^{T} = \begin{bmatrix} \mathcal{J}_{\alpha\alpha}\,\boldsymbol{D}^{xy} & \mathcal{J}_{\alpha\beta}\boldsymbol{D}^{xy} \\ \mathcal{J}_{\alpha\beta}\,\boldsymbol{D}^{xy} & \mathcal{J}_{\beta\beta}\boldsymbol{D}^{xy} \end{bmatrix}. \tag{66}$$

On the other hand, the intrinsic stiffness for the displacement-based formulation, $\mathbf{k}_{MP}$, may be evaluated directly using (13), which leads to the same expression (66). Similar equivalence can be also shown for the initial force vectors, showing in this way the equivalence of both formulations in the case of uniform stiffness along the element.

6 | GENERAL COMPARISON BETWEEN FORMULATIONS, AND NUMERICAL IMPLEMENTATION ASPECTS

6.1 | General comparison between displacement-based and hybrid mortar formulations

In the more general case (than that of Section 5) of linear elastic behavior but nonmatching nodes and/or nonuniform stiffness, the displacement-based and the hybrid formulations of the mortar element are not equivalent and they constitute two different approximations to the physical behavior of the contact/discontinuity surface. To better understand their differences, and the advantages and disadvantages of each of them, a comparison between the two formulations is presented in this subsection.

The key variables and relations involved in the displacement-based formulation of the mortar/interface elements (including traditional zero-thickness interface elements as a particular case), are represented in the scheme of Figure 5(A). The scheme is similar to the typical scheme for displacement-based continuum elements. It includes two levels of variables: the nodal level on top part of diagram with nodal displacements $\boldsymbol{u}^{el}$ and nodal forces $\boldsymbol{F}^{el}$, and the Gauss point level

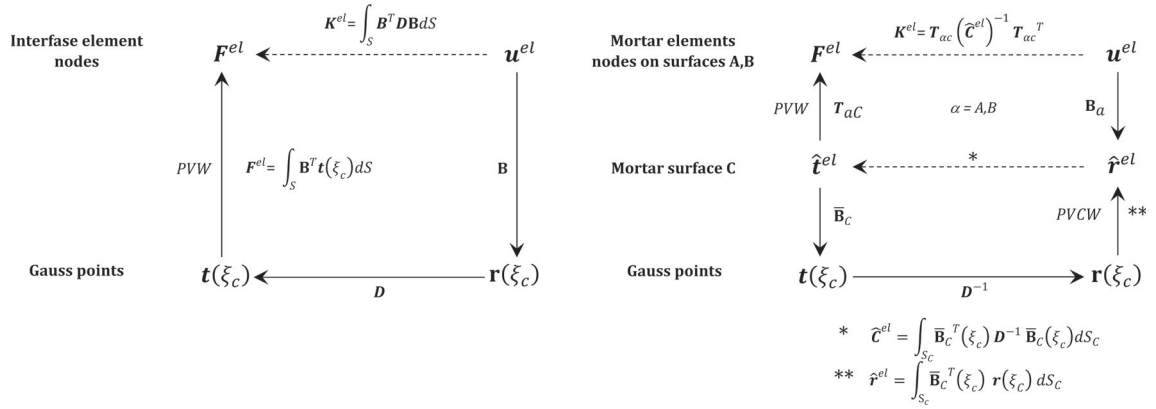

(A) Standard interface element formulation (B) Mortar hybrid interface element formulation

FIGURE 5 Standard and mortar hybrid interface scheme. (A) Standard interface element formulation and (B) mortar hybrid interface element formulation

at the lower part of diagram with "stresses" (stress tractions) and "strains" (relative displacements). The relations between those variables configure a logical path leading from nodal displacements to nodal forces: (i) from nodal displacements $\boldsymbol{u}^{el}$ one can evaluate displacements and "strain" (relative displacements in this case) at any point within the elements using the interpolation (matrices "N" and "B"), (ii) from "strain" one can then calculate stresses using he constitutive law and, finally, (iii) from stresses at all Gauss points, one can evaluate nodal forces for the element using the weak (integral) form of equilibrium Equation (8).

On the other hand, Figure 5(B) represents the counterpart scheme for the hybrid formulation. As seen in the figure, in this case the scheme turns out more complex, with an additional intermediate level of static and kinematic variables of the mortar surface, consisting of the "reduced" vectors of stress traction and relative displacement at the mortar surface nodes, $\hat{\boldsymbol{t}}^{el}$ and $\hat{\boldsymbol{r}}^{el}$. A "logical path" of kinematic and static relations leading unambiguously from the overall element displacements $\boldsymbol{u}^{el}$ to overall element forces $\boldsymbol{F}^{el}$, may be also identified in this case: (i) The displacement interpolation functions defined over the surfaces A and B provide a unique (strong) relation between overall nodal displacements $\boldsymbol{u}^{el}$ and mortar relative displacement vector $\hat{\boldsymbol{r}}^{el}$, (ii) the "reduced stiffness" matrix of the mortar surface relates $\hat{\boldsymbol{r}}^{el}$ with the corresponding reduced force vector $\hat{\boldsymbol{t}}^{el}$, and (iii) the transfer matrices $\mathbf{T}_{AC}$ and $\mathbf{T}_{BC}$ obtained via the PVW provide the relation between $\hat{\boldsymbol{t}}^{el}$ and the overall nodal element forces $\boldsymbol{F}^{el}$. But in this case, the reduced stiffness matrix involved in step (2) is not simply given by the constitutive equation, but is the result of the inversion of a reduced compliance matrix resulting from combination of three additional relations: (ii.1) the mortar interpolation of mortar stress tractions at any point $\boldsymbol{t}$ in terms of the reduced mortar forces $\hat{\boldsymbol{t}}^{el}$, (ii.2) the "compliance-based" constitutive relation between stress tractions $\boldsymbol{t}$ and relative displacements $\boldsymbol{r}$ at the same point of the mortar contact, and (ii.3) the weak kinematic relation based on the PCVW providing the reduced relative displacement vector of the mortar $\hat{\boldsymbol{r}}^{el}$ as an integral of the relative displacements along the mortar, $\boldsymbol{r}$.

6.2 | Numerical implementation for nonlinear constitutive laws

The numerical implementation of a finite element with nonlinear material laws generally involves two types of operations to be performed at each iteration of the calculation:

(a) Calculation of the stiffness matrix and initial force vectors of each element to be assembled and sent to the solver.
(b) Calculations after calling the solver and obtaining the new values of nodal displacements: (b.1) evaluation of the corresponding relative displacements ("strains") and stress tractions ("stresses") for the iteration, at each Gauss point of the mortar/interface elements, (b.2) using the constitutive equations to calculate the real "stress" (if the model is strain-prescribed) or "strain" (if the model is stress-prescribed) at the Gauss points, and (b.3) integrating those along

mortar surfaces C to obtain the real internal forces and stiffness of the elements that after being assembled lead to new global unbalanced forces and stiffness matrix for the following iteration.

In the case of displacement-based formulation, calculations included in "a)" may be done directly with the integral expressions (10) in the case of traditional interface elements with matching faces, or Equations (25)-(27) for mortar elements with unmatched faces. Calculations included in b) have to be performed in the sequence defined in Figure 5(A), which coincides with the sequence of steps (b.1)–(b.2)–(b.3) just described.

In the case of the hybrid formulation, the calculation sequence becomes a little longer. Calculations involved in "a)" include three steps: (i) first obtaining the reduced compliance matrix and initial relative displacement vector $\widehat{\mathbf{D}}^{el}$, $\widehat{\boldsymbol{t}}_0^{el}$ by integration over the mortar surface of $\widehat{\mathbf{C}}^{el}$, $\widehat{\boldsymbol{r}}_0^{el}$ and inversion via Equations (38) and (40), (ii) obtaining the transfer matrices $\mathbf{T}_{AC}$ and $\mathbf{T}_{BC}$ also by integration over the mortar surface via Equations (44) and (46) and, finally, (iii) making the necessary products of those matrices and vectors (53) to obtain the overall stiffness matrix and force vectors $\mathbf{K}^{el}$, $\boldsymbol{F}_0^{el}$.

Still for the hybrid formulation, calculations involved in "b)" include the following steps which are related to the scheme of Figure 5(B): (i) mortar relative displacement vector $\widehat{\boldsymbol{r}}^{el}$ is obtained from nodal displacements $\boldsymbol{u}^{el}$ using $\mathbf{B}_A(\xi)$, $\mathbf{B}_B(\xi)$, Equation (21), (ii) the reduced force vector $\widehat{\boldsymbol{t}}^{el}$ is obtained as the product of $\widehat{\boldsymbol{r}}^{el}$ with the reduced stiffness matrix $\widehat{\mathbf{k}}^{el}$, which was used for the element considered to construct the structural stiffness in step "a)," Equation (39), (iii) stress traction $\boldsymbol{t}$ at the Gauss points is obtained from $\widehat{\boldsymbol{t}}^{el}$ via interpolation functions $\overline{N}_C$ and rotation matrix $\mathbf{R}$, Equation (31), and (iv) relative displacements $\boldsymbol{r}$ are obtained from stress tractions $\boldsymbol{t}$ by multiplying by the constitutive compliance matrix $\boldsymbol{D}^{-1}$, which was used for the element and Gauss point considered to construct the element reduced compliance and stiffness matrices, Equation (36). This completes step "b.1)." Once $\boldsymbol{t}$ are $\boldsymbol{r}$ known, the constitutive equation is called to obtain a new stress-strain state that will satisfy the material laws and the new constitutive stiffness or compliance (step "b.2)"). Finally, in step "b.3)" integration of the relative displacements $\boldsymbol{r}$ along the mortar surface leads to the reduced vector of nodal relative displacements $\widehat{\boldsymbol{r}}^{el}$ (35), integral Equation (38) leads to the new reduced compliance and then stiffness matrix $\widehat{\mathbf{k}}^{el}$, multiplication by $\widehat{\boldsymbol{r}}^{el}$ to the reduced nodal tractions $\widehat{\boldsymbol{t}}^{el}$ (39), and integration over the mortar surface leads to the final vector of nodal forces (43) and (45).

In the workflows just described, note that the displacement-based formulation fits more naturally with constitutive equations which are strain-driven, while the hybrid formulation fits better with constitutive equations that are stress-driven. This is because strain-driven constitutive formulations provide directly the new stress and the new stiffness for prescribed strain values, and these are precisely the inputs required for the evaluation of integrals (10) or (25)-(27). By contrast, stress-driven constitutive equations (such as viscoplasticity, see for instance Aliguer et al.[30]) provide naturally strain and constitutive compliance for prescribed stress increments, which are the inputs required to calculate the reduced vector of mortar relative displacements and the reduced compliance (38).

The fact that the constitutive compliance matrix $\boldsymbol{C} = \boldsymbol{D}^{-1}$ is required in the integral expression (38), also sets another significant limitation for the hybrid formulation: the constitutive compliance has to exist, which means that constitutive stiffness has to be invertible and therefore it cannot be singular or exhibit negative eigenvalues. This means that for instance, classical elastoplasticity with softening would not seem an acceptable model for this formulation, unless an "ad hoc" procedure is established to modify the tangent stiffness so that it remains positive and invertible at all times (although this arbitrary procedure may have other unpredictable effects in terms of convergence). By contrast, viscoplastic models would always seem adequate for hybrid formulations, since they may be always written to provide a consistent compliance matrix for the time increment.[30]

6.3 | Nonlinear mortar/interface constitutive laws

In this study, two constitutive models have been used to represent the behavior of the discontinuity/contact surface represented by the mortar/interface element, one is relative-displacement ("strain")-driven elastoplastic model, and the other one is stress-driven viscoplasticity.

The "strain"-driven law is an existing and extensively verified normal/shear cracking constitutive model that incorporates fracture mechanics concepts and parameters.[28,29] The initial loading surface is a hyperbola (Figure 6(A), curve "0") defined in terms of the normal and shear stresses on the discontinuity plane σ_N, σ_T, and characterized by three geometric parameters: friction angle φ, cohesion c and tensile strength χ, according to the expression:

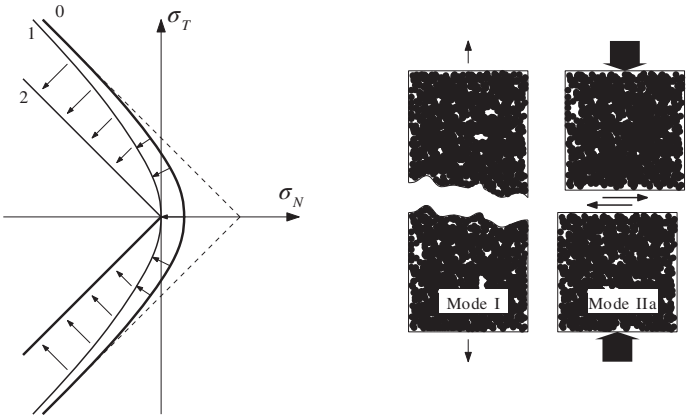

(A) Evolution of cracking surface (B) Fundamental modes of fracture

FIGURE 6 Hyperbolic cracking model

$$F(\boldsymbol{\sigma}) = -(c - \sigma_N \tan\varphi) + \sqrt{\sigma_T^2 + (c - \chi \tan\varphi)^2}. \tag{67}$$

The model covers the full range of mixed-mode cracking, with the two limit cases that correspond to the two fundamental fracture modes: (i) Mode I cracking under pure tension with zero shear stresses when the surface is reached along the horizontal axis and (ii) Mode IIa ("asymptotic" mode II) cracking under shear and very high compression when the surface is reached in its asymptotic region, where the hyperbola approaches a Coulomb criterion (Mode IIa), as depicted in Figure 6(B).

Once the stresses reach the initial loading surface and cracking is initiated, the loading surface starts shrinking. The evolution of its geometric parameters is controlled by a single history variable: the work spent in fracture processes, W^{cr}, the evolution of which is defined incrementally as the plastic work (in tension), or the plastic work less a basic friction work (in shear-compression). As W^{cr} grows, the values of tensile strength χ and cohesion c decay according to the softening laws, which are defined in such a way that tensile strength χ vanishes when W^{cr} reaches the value of the fracture energy in mode I, $G_F{}^I$, and cohesion c vanishes when W^{cr} reaches the value of the fracture energy in mode IIa, $G_F{}^{IIa}$, being these fracture energies two of the model parameters. In this way, as the fracture process progresses, the loading surface in Figure 6(A) evolves from configuration "0" (initial surface) to "1" (surface when the tensile strength is exhausted but the crack surface is still rough, typical situation after pure tensile cracking) and depending on the type of loading, eventually to "2" (totally degraded state of the crack, in which no roughness remains, situation only attainable under shear/compression). Additional details of the constitutive model and results obtained in basic loading situations may be found in Carol et al.[28] and Caballero et al.[29]

The "stress"-driven law, on its side, is a perfect viscoplastic model defined on the basis of the same hyperbolic loading surface. The theory and implementation details as well as simple examples of application may be found in Aliguer et al.[30]

6.4 | Numerical integration over the mortar/interface elements

The integrations necessary to calculate all matrices and vectors of the mortar/interface elements, such as $\mathbf{k}_{AA}$, $\mathbf{k}_{AB}$, $\mathbf{k}_{BA}$, $\mathbf{k}_{BB}$ (26); $\boldsymbol{f}_{A0}, \boldsymbol{f}_{B0}$ (27); $\hat{\mathbf{C}}^e$, $\hat{\boldsymbol{r}}_0^{el}$ (38); $\mathbf{T}_{AC}$ (44) or $\mathbf{T}_{BC}$ (46), are carried out numerically over the mortar surface C using the trapezoidal integration rule, that is, using the two end points of the midplane surface C of each mortar/interface element, and equal weighs. In the case of traditional interface elements, the integration rules with integration points in between each pair of nodes were shown to lead to stiffness matrices with diagonal structure that minimizes the coupling between the nodes, and therefore reduce the jumps or oscillations in the results related to the development and evolution of sharp sliding fronts.[2,35] In the case of the mortar/interface elements, the nodes on both sides A and B are no longer facing each other; however, the concept has been equally applied to surface C, with satisfactory results as it will be seen in the application examples in the following section.

7 | EXAMPLES OF APPLICATION

7.1 | Example 1

The first example consists of a direct shear test or a rectangular specimen of dimensions 12×8 m. The specimen is formed by two horizontal layers of the same thickness and the same elastic material which are discretized with different, nonmatching meshes. These two layers are separated by a surface of 11 zero-thickness mortar/interface elements as represented in Figure 7. During the first loading step, vertical stress is applied on the top of the mesh, while the bottom remains fixed vertically and the laterals are left free to expand horizontally. The second loading step consists of adding an increasing tangential displacement up to 0.1 m applied on the nodes on the upper side of the mortar/interface surface, while fixing the horizontal movement of the lower nodes of the same elements. The test is repeated for different, progressively increasing values of the vertical load applied during the first load step.

The first series of results in this example are obtained using for the mortar/interface elements the displacement-based formulation of Section 3, and the elastoplastic constitutive law described in Section 6.3. The constitutive parameter values used for the continuum are E = 250 MPa and $\nu = 0.2$, and for the interface: normal and tangential elastic stiffness $K_N = K_T = 25{,}000$ MPa/m, initial friction angle $\tan\phi_0 = 0.8785$, initial tensile strength $\chi_0 = 3.0$ MPa, initial cohesion $c_0 = 4.5$ MPa, fracture energy mode I, $G_F{}^I = 0.03$ MPa·m, energy mode IIa, $G_F{}^{IIa} = 0.06$ MPa·m and normal stress at which dilatancy vanishes, $\sigma_{dil} = 20$ MPa.

The results of this example are depicted in Figures 8 and 9. In Figure 8, the evolution of the shear stress versus the shear relative displacement is represented for different values of the applied normal stress, at a point of mortar/interface. As it should be expected in this case of uniform stresses, the family of shear softening curves obtained reproduce exactly the constitutive behavior. After the initial elastic response till the stress peak, the curves show a postpeak behavior with softening which is progressively less steep and approaches asymptotically a horizontal line representing residual friction. The peak and residual stress values for different curves are higher for higher normal stress. The descending curves show a little slope discontinuity corresponding to the point at which the history variable W^{cr} reaches the value of energy fracture mode I, $G_F{}^I$, for which the tensile strength parameter χ vanishes. After that, shear stress decreases at a slower pace while the history variable continues increasing toward the mode IIa fracture energy value, $G_F{}^{IIa}$.

Figure 9 represents the evolution of the normal relative displacement (dilatancy) versus the prescribed shear relative displacement, for different values of the applied normal stress. It can be seen that dilatancy is lower for higher values of the normal stress applied.

The calculation of Example 1 is repeated again, but now for a single value of normal stress 10 MPa, and considering the hybrid formulation of the mortar/interface element and the elastic-perfectly viscoplastic constitutive model. The parameter values used for the continuum are the same as before. For the viscoplastic interface law, most parameters which are common to the previous elastoplastic law are given also the same values ($K_N = K_T = 25{,}000$ MPa/m, friction angle $\tan\phi_0 = 0.8785$, cohesion $c_0 = 4.5$ MPa), except the initial tensile strength which is assumed to be zero ($\chi_0 = 0$). The viscosity parameter value is taken as $\eta = 10^6$ MPa·s. The loading history is accommodated to the nature of the

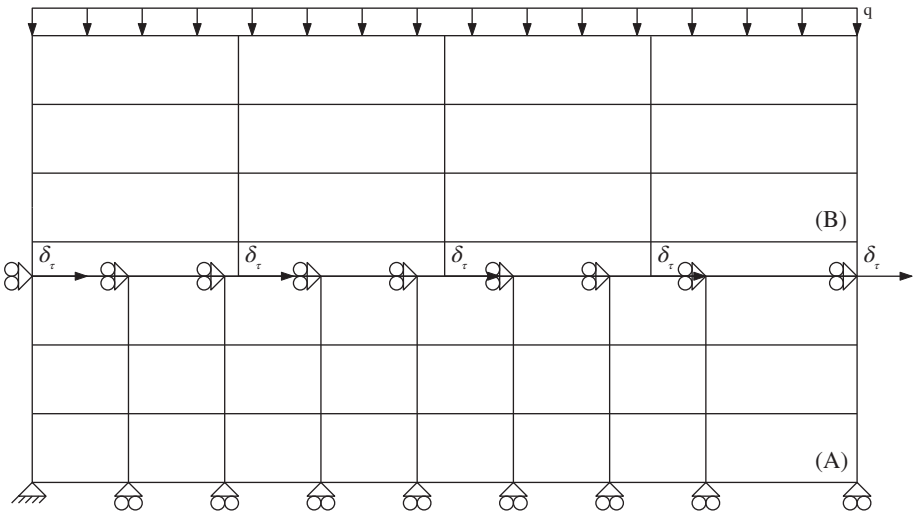

FIGURE 7 Direct shear under constant compression: Geometry and boundary conditions

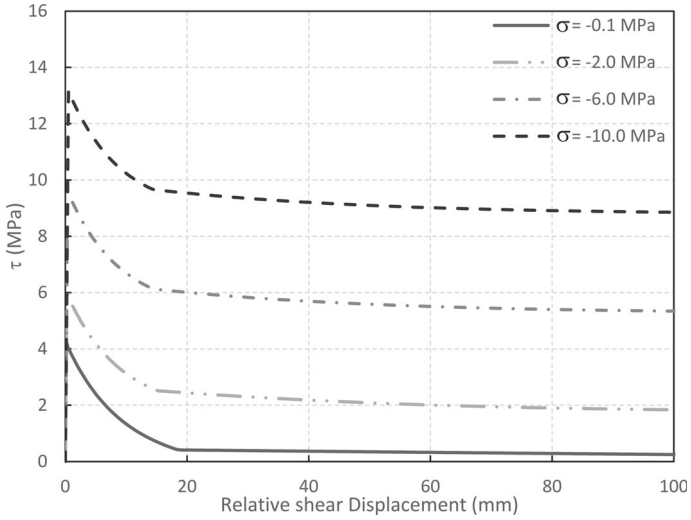

FIGURE 8 Results of the shear test: shear traction versus relative shear displacement, for different values of σ

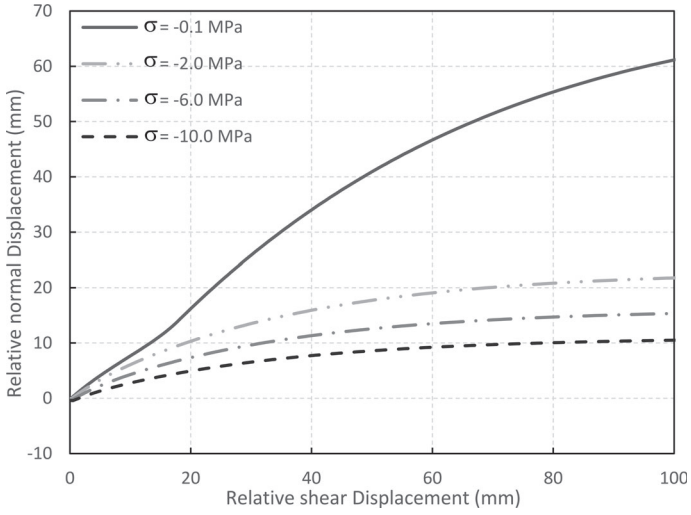

FIGURE 9 Results of the shear test: normal opening displacement versus shear displacement, for different values of σ

viscoplastic constitutive model. Each increment of the tangential displacement is applied instantaneously and is followed by a number of time increments until stress stabilizes.

Figure 10 depicts the results of this calculation, together with the results obtained with the previous displacement-based mortar formulation and the elastoplastic model with equivalent parameters (perfect elasto-plasticity). Figure 10(A) depicts the shear stress evolution with the prescribed shear relative displacements. As expected, after each elastic increment, the relaxation that takes place during the viscoplastic time steps takes shear stress down to the inviscid elastoplastic response limit. Figure 10(B) represents the normal and shear stress profiles obtained along the specimen interface (normal stress is the bottom line; shear stress is the top line).

Note that, although loading and constitutive behavior are very simple, the above calculations involve nonmatching meshes using both mortar formulations and different constitutive models. In spite of that, the results turn out perfectly smooth without any spurious oscillation or anomalies, and viscoplastic results coincide with perfect elastoplasticity as they should in the limit case of sufficient time elapsed after each load increment.

7.2 | Example 2

The second example consists of a 2×4 m vertical specimen with an inclined discontinuity crossing the specimen at 45°, and nonmatching meshes on both sides of the discontinuity leading to three mortar/interface elements,

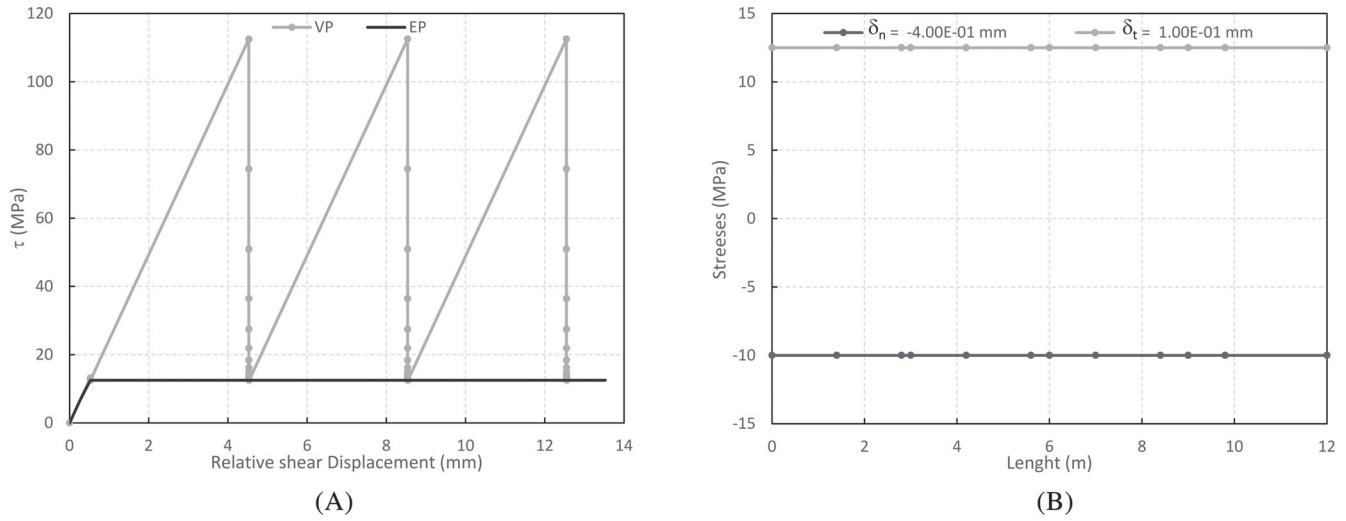

FIGURE 10 Results of the hybrid mortar formulation and viscoplastic constitutive law, for the shear test with 10 MPa normal stress: (A) shear stress traction versus relative displacements, and comparison to similar results obtained with the displacement-based formulation and perfect elastoplasticity and (B) normal and shear stress profiles obtained along the mortar surface at the end of the test

see Figure 11. The specimen is subject to a triaxial stress state created by a constant horizontal confinement distributed loads, and a variable vertical load which is applied via progressively increasing vertical displacement of negative sign prescribed at the top face of specimen. Various values are considered for the horizontal confinement.

Same as in the previous example, the continuum elements are assumed linear elastic with $E = 10^5$ MPa and $\nu = 0.2$, and calculations are repeated using two different assumptions for the mortar/interface elements: (i) displacement-based formulation of the mortar elements equipped with elastoplastic constitutive model with softening and (ii) hybrid mortar element with perfect viscoplasticity.

In the first case, the mortar/interface constitutive parameters are: normal and tangential elastic stiffness $K_N = K_T = 10^7$ MPa/m, initial friction angle $\tan\phi_0 = 0.8785$, initial tensile strength $\chi_0 = 3.0$ MPa, initial cohesion $c_0 = 4.5$ MPa, fracture energy mode I, $G_F{}^I = 0.5$ MPa·m, fracture energy mode IIa, $G_F{}^{IIa} = 5$ MPa·m and normal stress at which dilatancy vanishes, $\sigma_{dil} = 0$ MPa. The results obtained for various confinement levels (q): 0%, 5%, 10% and 20% of the uniaxial compressive strength value of the specimen 36.65 MPa, are depicted in Figures 12, 13 and 14.

Figure 12 shows the evolution of the total vertical force against the vertical prescribed displacement, for the various levels of confinement (note specimen width 2 m.). The initial elastic response ends when the peak strength of the discontinuity is reached, followed by postpeak softening response.

Figure 13(A,B) depict the evolution of shear and normal stresses on the discontinuity surface vs the corresponding shear and normal relative displacements, for the various levels of lateral confinement. In contrast to Example 1, in this case normal stresses on the discontinuity are not statically determined by fixed external loading values, but are an outcome of the structural calculation, and similarly are shear stresses. Due to equilibrium considerations, however, the values of shear and normal stresses have to be in a constant proportion given by the discontinuity angle.

Similar to the previous section, Example 2 is also solved using the hybrid formulation of the mortar/interface element with perfect viscoplasticity, for the cases of no confinement and 20% confinement. The results are represented in Figures 14 and 15, together with the same curves obtained with the displacement-based formulation and perfect elastoplasticity. The parameter values are the same as in Example 1 and, also in this case, each increment of the vertical displacement is applied instantaneously and followed by a number of time increments until the solution becomes stationary. Figure 14 represents the evolution of the total vertical force against prescribed displacement applied on the specimen, and Figure 15 the evolution of shear stress on the discontinuity surface vs the corresponding shear relative displacements, for the two levels of lateral confinement.

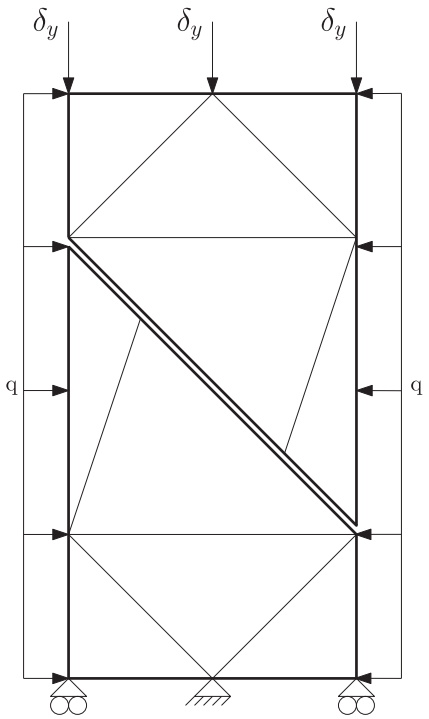

FIGURE 11 Specimen with inclined discontinuity: geometry and boundary conditions

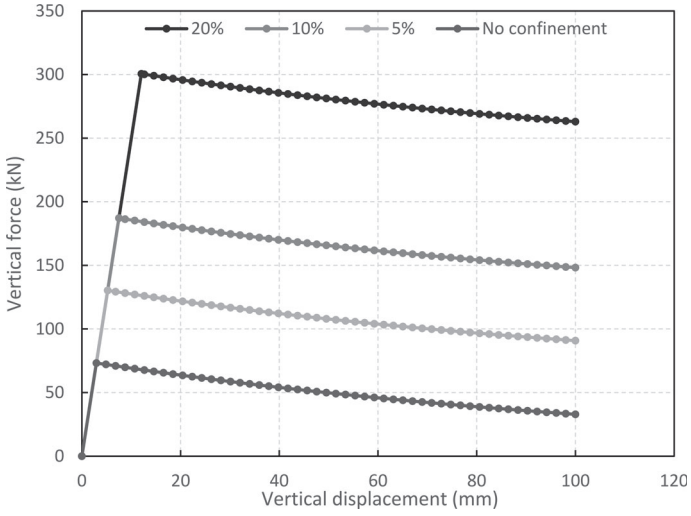

FIGURE 12 Specimen with inclined discontinuity: vertical force versus vertical displacement, for different values of lateral confinement, given as the percentage of the specimen uniaxial compression strength (note specimen width 2 m)

The curves show that, after each instantaneous elastic load increment, the pass of time and the corresponding viscoplastic deformations cause the stress to relax and progressively approach their inviscid elastoplastic limit. Note that in this case, the stress relaxation paths do not follow vertical lines as in Example 1 but inclined lines; this is due to the structural (statically undetermined) configuration. The results obtained show that, also in this second example involving a structural response, the two formulations lead to smooth results in spite of the nonmatching meshes.

7.3 | Example 3

Aiming at geomechanical applications, the third example corresponds to a soil reinforcement pull-out test consisting of a rectangular soil domain, with a thin steel layer sitting on top which is first compressed against the soil, and then pulled out laterally from the left side. In between soil and reinforcement, a discontinuity or contact is assumed with basic

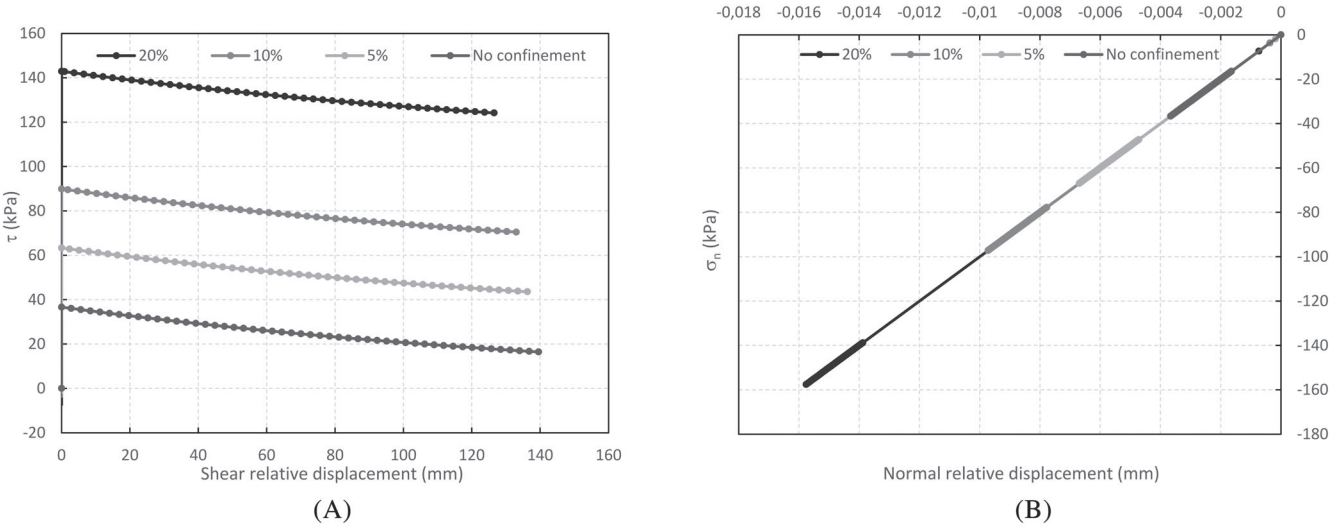

FIGURE 13 Specimen with inclined discontinuity: (A) shear stress versus shear relative displacement and (B) normal stress versus normal relative displacement, both on the discontinuity plane and for different values of lateral confinement

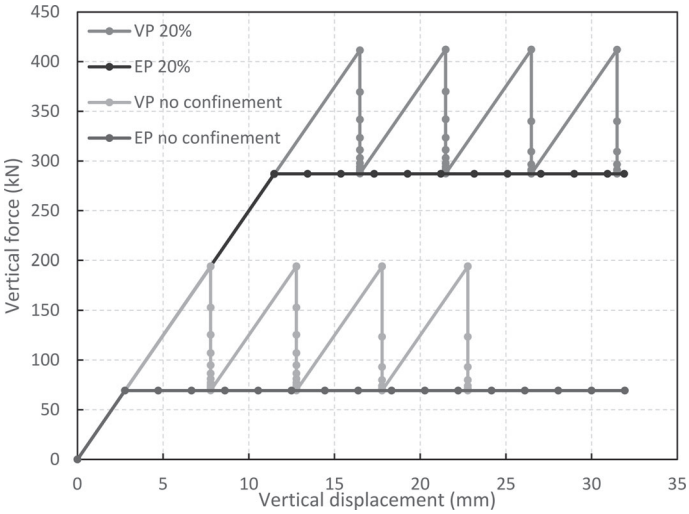

FIGURE 14 Results of hybrid formulation with perfect viscoplasticity: vertical force versus vertical displacement for different values of lateral confinement, and comparison to the displacement-based formulation with perfect elastoplasticity

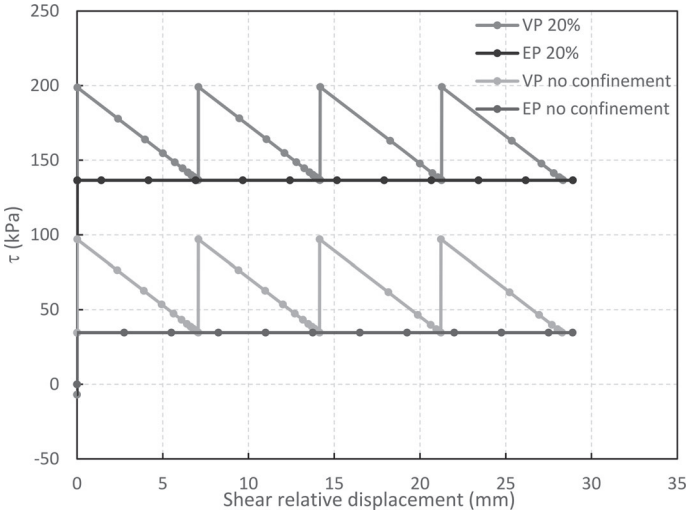

FIGURE 15 Results of hybrid formulation with perfect viscoplasticity: shear traction versus relative shear displacement, and comparison to the displacement-based formulation with perfect elastoplasticity

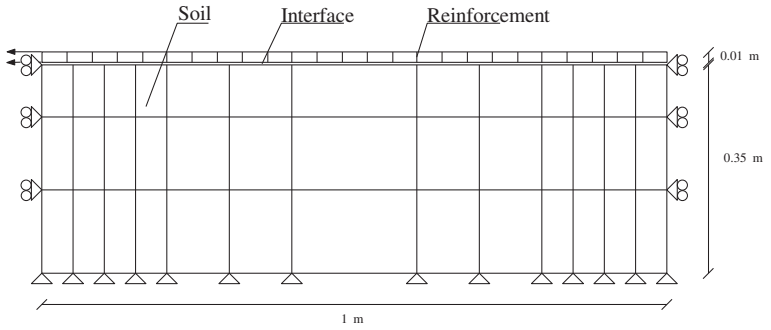

FIGURE 16 Pull-out test: Geometry and boundary conditions

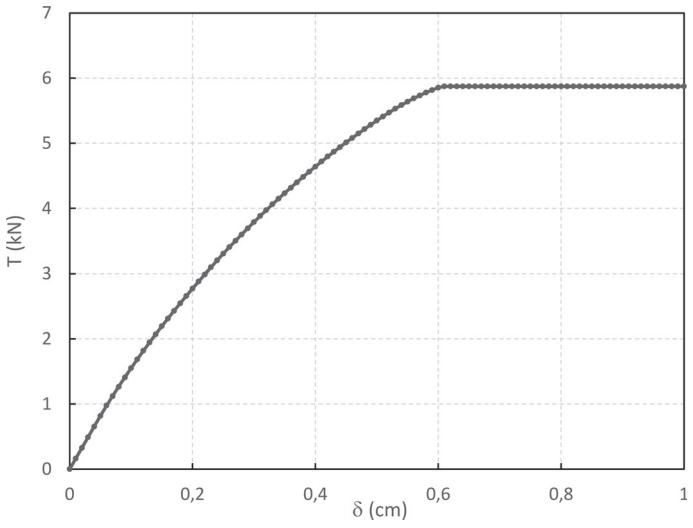

FIGURE 17 Results of the pull-out test: load–displacement curve

frictional behavior, see Figure 16. This example was used in early papers on traditional zero-thickness interface elements with matching meshes.[2] In the present calculations, however, the meshes for soil and reinforcement are nonmatching, and the contact is represented by 33 mortar/interface elements. Although normal stress on the interface is practically prescribed, the main difference with the previous two examples is the nonuniform distribution of shear stresses and relative displacements along the discontinuity, and the emergence of a sharp sliding front that moves progressively from left to right as the reinforcement is being pulled out from the left. All these make this problem a nontrivial case suitable to test the performance of the mortar/interface element formulations proposed.

Soil and reinforcement are both assumed linear elastic materials with elastic moduli $E_s = 1$ MPa for soil, and $E_r = 100$ MPa for reinforcement, and Poisson ratio $\nu = 0.3$ for the soil, and zero for steel (this just for convenience, in this way shear stresses between soil and steel will remain strictly zero during the first loading step with normal loading, as described below). For the mortar elements, the displacement-based formulation is used, with perfect elastoplastic frictional behavior with the following interface constitutive parameters: elastic stiffness $K_N = K_T = 10$ MPa/m, friction angle tangent $\tan\phi_0 = 0.57735$, asymptotic cohesion $c_0 = 0.1$ kPa and zero tensile strength $\chi_0 = 0.0$ kPa. In the model used (described in Section 6.3), perfect elastoplasticity is recovered for very high fracture energy values, here $G_F^I = 100$ MPa·m, and $G_F^{IIa} = 1000$ MPa·m are adopted and, finally, the normal stress at which dilatancy vanishes, $\sigma_{dil} = 10$ kPa.

As already mentioned above, the loading sequence consists of first applying a vertical load on top of the steel layer, of value 10 MPa. Then the second load step consists of prescribing increasing value of horizontal displacements to the left end face of the steel layer. The results of the analysis are shown in Figures 17, 18, and 19. In Figure 17, the total force applied on the left end of the steel reinforcement (sum of nodal reactions on the nodes with prescribed displacements), is represented against the displacement values prescribed. The total force increases at a progressively slower rate as a larger part of the contact is sliding, until reaching a maximum value, which corresponds to the final stage in which the entire contact surface is sliding. This limit value corresponds very well to the product of the contact area times the shear stress that by friction corresponds to the normal stress applied on the steel.

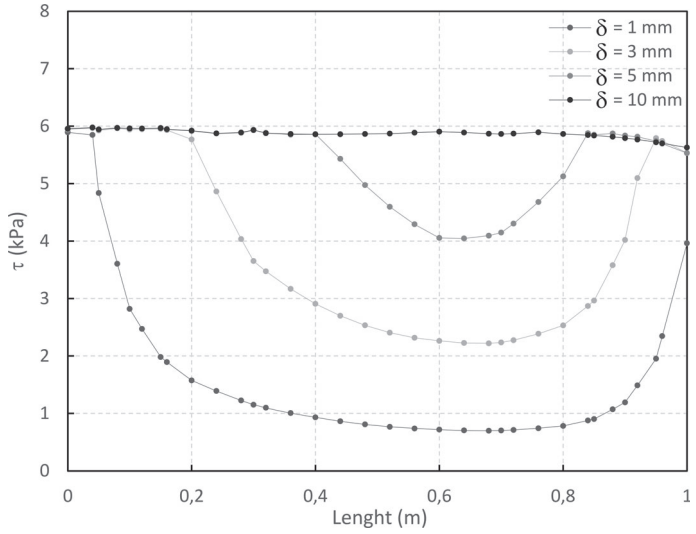

FIGURE 18 Results of pull-out test: distribution of shear stresses along the contact surface

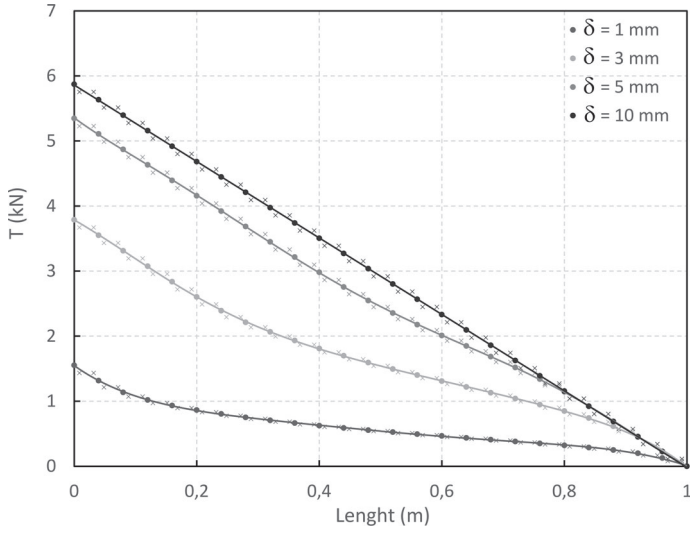

FIGURE 19 Results of the pull-out test: distribution of total axial force along the reinforcement

Figure 18 depicts the shear stress distribution along the contact surface, showing that higher shear stresses take place and sliding indeed starts at the left end of the reinforcement layer, but they also reach a second maximum and start early sliding at the opposite (right) end (this effect is caused by the steel layer being free on its right end and much stiffer than the soil, together with the fact that the soil layer is assumed anchored to the vertical right boundary; similar shear stress profiles were reported in early calculations of this problem using traditional interface elements[2]). Shear stress profiles at later stages of the pull-out show as the central part of the reinforcement has a minimum shear stress level that progressively increases till the final situation in which the whole contact surface is in sliding condition.

As a final result of this example, Figure 19 represents the profiles at different times of the total axial force transmitted by the reinforcement. These forces are obtained using two different procedures: (1) indicated by crosses are the forces obtained as the integral of σ_{xx} across the steel reinforcement cross-section and (2) as dots connected by solid lines are the forces resulting from summing appropriate nodal forces on individual elements of the steel layer which can be obtained by postprocessing. As seen in the figure, the results obtained by the two methods are basically coincident except for the little differences due to the fact that elements are linear and stress at Gauss points do satisfy equilibrium in a weak (average) sense, which causes stresses to be constant within the element, while nodal forces do satisfy equilibrium in the strict sense and therefore lead to a continuous line. Overall, the force profiles shown in the figure seem totally consistent with the shear stress distributions above, since the variation of the steel axial force from one cross-section to the next has to be in equilibrium with the shear stress applied by frictional contact with the soil base. Therefore, the slope at any point of the axial force diagram of Figure 19, has to be proportional to the shear stress value at the same point in Figure 18.

This seems satisfied, leading, in the final situation of sliding all along the reinforcement with constant shear stress, to a straight line with constant slope of the axial force diagram.

A final series of calculations of this example have been run to investigate the comparison of using a matched mesh with traditional zero-thickness interface elements, and also the effect of mesh size. To this end, the various meshes represented in Figures 20 and 21 have been considered. Note that the coarsest unmatched mesh is the one already used in previous calculations.

FIGURE 20 Various mesh sizes used in the calculations

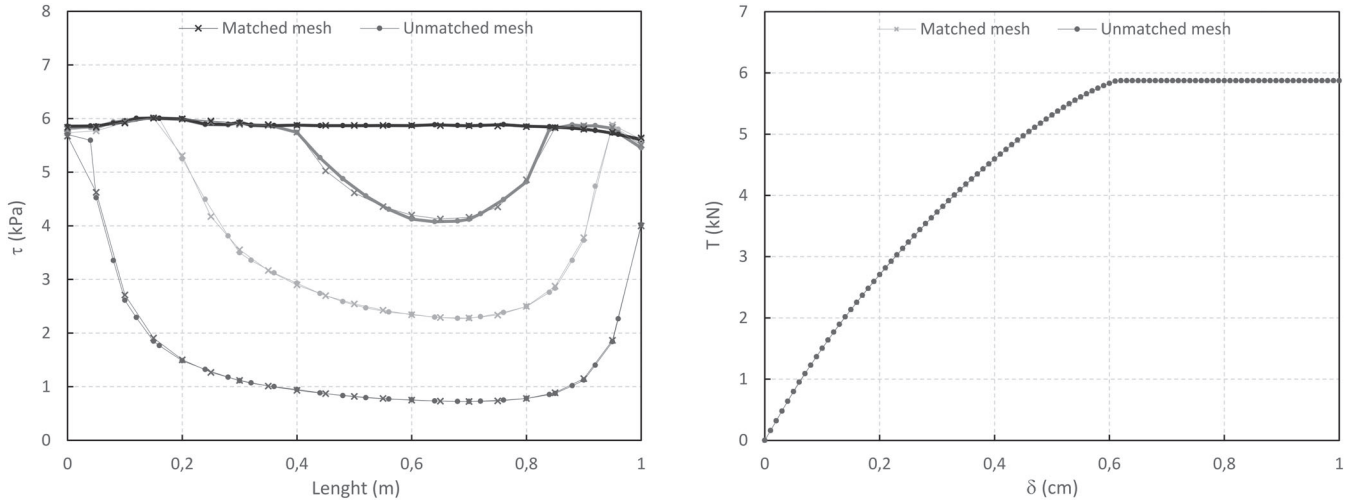

FIGURE 21 Comparison of results obtained with matched and unmatched meshes of coarsest size, of (left) tau distributions along contact, and (right) force-displacement diagram

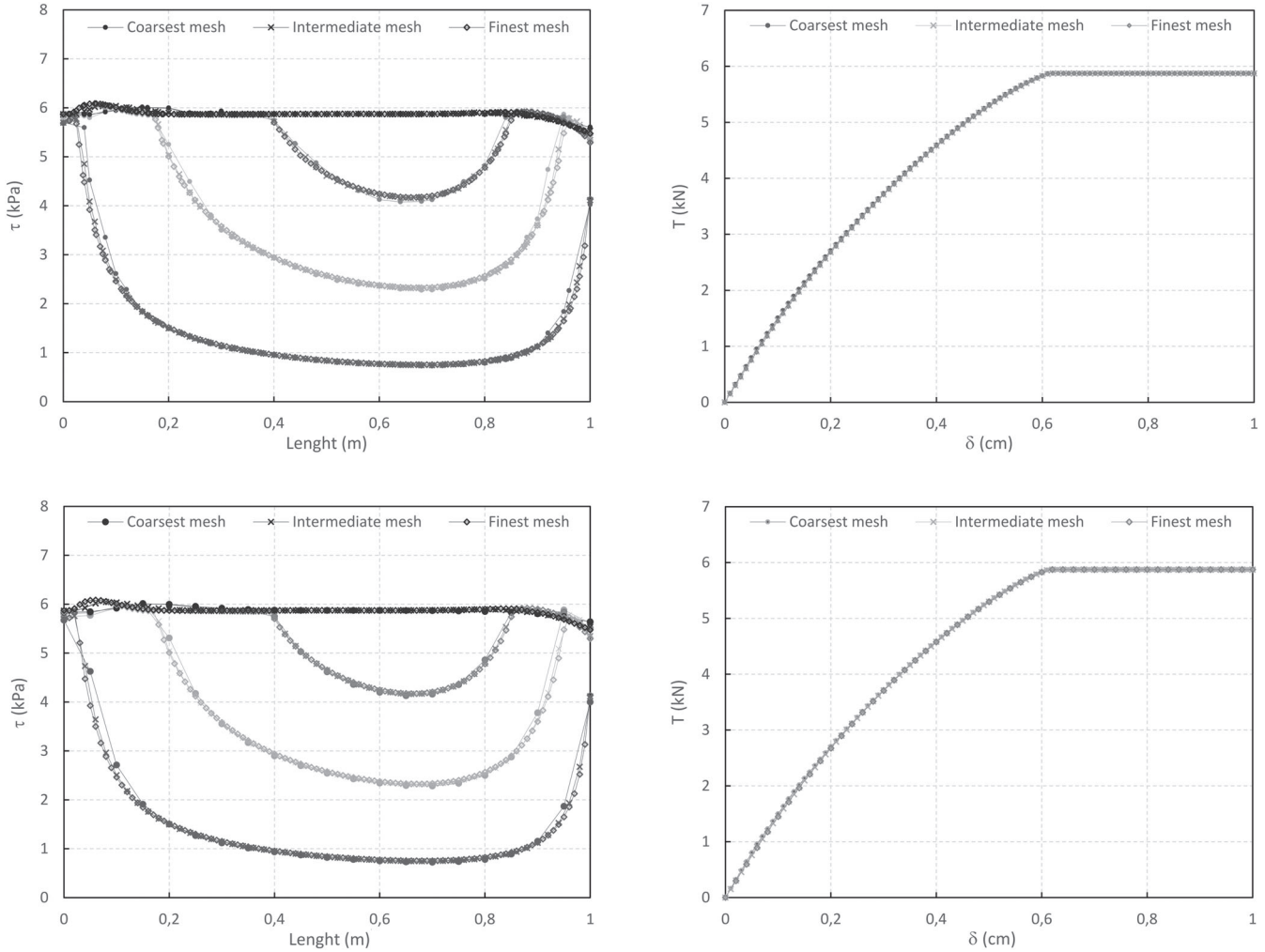

FIGURE 22 Comparison of results obtained with different sizes of (top) unmatched meshes and (bottom) matched meshes, of (left) tau distributions along contact, and (right) force-displacement diagram

The comparison of the results obtained using the various meshes of Figure 20 are shown in Figures 21 and 22. In Figure 21, the tau stress profiles and load-displacement curves obtained with the coarsest meshes using matched and unmatched nodes are represented together. In Figure 22, the same is done for the three matched meshes, and also for the three unmatched meshes.

As clearly seen in the comparison diagrams, the results are quite coincident and therefore do not seem exhibit mesh sensitivity except for minor details linked to the spatial resolution of each mesh along the contact surface.

8 | CONCLUDING REMARKS

A mortar/interface element with unmatched nodes has been formulated. The mortar/interface elements are not arbitrarily attached to any of the two side surfaces in contact, but they are the smallest segments resulting from the projection of the two surfaces on an independent intermediate mortar surface. In this way, a symmetric treatment is ensured of the mortar/interface formulation w.r.t. both surfaces in contact. The new element formulation has been developed in two different versions: (i) a displacement-based formulation which is more adequate to be combined with (strain-driven) elastoplastic interface constitutive models and (ii) a hybrid formulation which is more adequate to be combined with (stress-driven) viscoplasticity. The displacement-based formulation may be considered an extension of the traditional

zero thickness element formulation to the case of unmatched nodes, and the numerical implementation scheme may also be similar to classical interface elements. On the other hand, the new hybrid formulation may be seen as a dual formulation in which stress is interpolated along the contact surface rather than relative displacements, which leads to a more complex implementation scheme. Both formulations have been proven to be equivalent to each other in the particular case of linear elasticity and constant stiffness. In the first and second examples of application, the two formulations have been tested numerically, leading to smooth stress distributions with the expected values for all variables. The third example is a less trivial pull-out test leading to nonuniform state of shear stresses along the contact surface, and a sharp moving slide front moving along the contact surface. The results obtained in this case seem to capture well the sliding front and also lead to smooth stress profiles. A study of mesh size and comparison with traditional zero thickness interface elements with matched nodes, has also been carried out for this example, with the conclusions that: (1) the quality of the solution using the new mortar/interface elements with unmatched meshes is similar as using classical interface elements and matched meshes and (2) both approaches seem free of mesh sensitivity in the classical sense of element size.

ACKNOWLEDGEMENTS

This research has been supported by grants BIA2016-76543-R from MEC (Madrid), which includes FEDER funds, and 2017SGR-1153 from AGAUR-Generalitat de Catalunya (Barcelona). Miguel de Francisco also acknowledges the doctoral fellowships FI-2015 from AGAUR-Generalitat de Catalunya (Barcelona) and FPU15/02577 from MEC (Madrid).

REFERENCES

1. Goodman RE, Taylor RL, Brekke T. A model for the mechanics of jointed rock. *ASCE J Soil Mech Found Div*. 1968;94:637-659.
2. Gens A, Carol I, Alonso EE. An interface element formulation for the analysis of soil-reinforcement interaction. *Comput Geotech*. 1988;7:133-151.
3. Rots JG. Computational Modelling of Concrete Fracture [PhD thesis]. Delft: Delft University of Technology; 1988.
4. Segura JM, Carol I. Numerical modelling of pressurized fracture evolution in concrete using zero-thickness interface elements. *Eng Fract Mech*. 2010;77:1386-1399. https://doi.org/10.1016/j.engfracmech.2010.03.014.
5. Xujiang C, Lehua Q, Wenlong T, Kaike Y, Hejun L. Evaluation for interfacial fracture of fiber-reinforced pyrocarbon matrix composites by using a zero thickness. *J Alloys Compd*. 2020;820:153378. https://doi.org/10.1016/j.jallcom.2019.153378.
6. Ural A, Mischinski S. Multiscale modeling of bone fracture using cohesive finite elements. *Eng Fract Mech*. 2013;103:141-152. https://doi.org/10.1016/j.engfracmech.2012.05.008.
7. Hashagen F, de Borst R. An interface element for modelling the onset and growth of mixed-mode cracking in aluminium and fibre metal laminates. *Struct Eng Mech*. 1997;5(6):817-837. https://doi.org/10.12989/sem.1997.5.6.817.
8. Garolera D, Carol I, Papanastasiou P. Micromechanical analysis of sand production. *Int J Numer Anal Methods Geomech*. 2019;43:1207-1229. https://doi.org/10.1002/nag.2892.
9. Cerfontaine B, Dieudonné A-C, Radu JP, Collin F, Charlier R. 3D zero-thickness coupled interface finite element: formulation and application. *Comput Geotech*. 2015;69:124-140. https://doi.org/10.1016/j.compgeo.2015.04.016.
10. Dean RH, Gai X, Stone CM, Minkoff SE. A comparison of techniques for coupling porous flow and geomechanics. *SPE J*. 2006;11(1):132-140. https://doi.org/10.2118/79709-PA.
11. Meng J, Huang J, Sloan SW, Sheng D. Discrete modelling jointed rock slopes using mathematical programming methods. *Comput Geotech*. 2018;96:189-202. https://doi.org/10.1016/j.compgeo.2017.11.002.
12. Petrov VA, Leksin AB, Pogorelov VV, et al. Geodynamic simulation of ore-bearing geological structural units by the example of the Strel'tsovka uranium ore field. *Geologiya Rudnykh Mestorozhdenii*. 2017;59(3):173-200. https://doi.org/10.1134/s1075701517030047.
13. Maday Y, Mavriplis C, Patera AT. Nonconforming mortar element methods: application to spectral discretizations. In: Chan T, Glowinski R, Périaux J, Widlund OB, eds. *Second International Conference on Domain Decomposition*. Philadelphia, PA: SIAM; 1988.
14. Anagnostou G, Maday Y, Mavriplis C, Patera AT. On the mortar element method: generalizations and implementation. In: Glowinski R, ed. *Third International Conference on Domain Decomposition Methods for Partial Differential Equations*. Philadelphia, PA: SIAM; 1990.
15. Bernardi C, Maday Y, Patera AT. A new nonconforming approach to domain decomposition: the mortar element method. In: Brezis H, Lios JL, eds. *Nonlinear Partial Differential Equations and their Applications*. Pitman: Collège de France Seminar XI; 1994;13–51.
16. Wohlmuth BI, *Discretization Methods and Iterative Solvers Based on Domain Decomposition*. Berlin Heidelberg: Springer; 2001.
17. Puso MA, Laursen TA. A mortar segment-to-segment contact method for large deformation solid mechanics. *Comput Methods Appl Mech Eng*. 2004;193:601-629. https://doi.org/10.1016/j.cma.2004.06.001.
18. Yang B, Laursen TA, Meng XN. Two dimensional mortar contact methods for large deformation frictional sliding. *Int J Numer Methods Eng*. 2005;62:1183-1225. https://doi.org/10.1002/nme.1222.
19. Fischer KA, Wriggers P. Frictionless 2D contact formulations for finite deformations based on the mortar method. *Comput Mech*. 2005;36:226-244. https://doi.org/10.1007/s00466-005-0660-y.
20. Yang B, Laursen TA. A large deformation mortar formulation of self-contact with finite sliding. *Comput Methods Appl Mech Eng*. 2008;197:756-772. https://doi.org/10.1016/j.cma.2007.09.004.

21. McDevitt TW, Laursen TA. A mortar-finite element formulation for frictional contact problems. *Int J Numer Meth Eng*. 2000;48:1525-1547.
22. Camacho GT, Ortiz M. Computational modelling of impact damage in brittle materials. *Int J Solid Struct*. 1996;33(20–22):2899-2938.
23. Pandolfi A, Ortiz M. An efficient adaptive procedure for three-dimensional fragmentation simulations. *Eng Comput*. 2002;18(2):148-159.
24. Mergheim J, Kuhl E, Steinmann P. A hybrid discontinuous Galerkin/interface method for the computational modelling of failure. *Commun Numer Methods Eng*. 2004;20:511-551. https://doi.org/10.1002/cnm.689.
25. Radovitzky R, Seagraves A, Tupek M, Noels L. A scalable 3D fracture and fragmentation algorithm based on a hybrid, discontinuous Galerkin, cohesive element method. *Comput Methods Appl Mech Eng*. 2011;200:326-344. https://doi.org/10.1016/j.cma.2010.08.014.
26. Nguyen VP, Nguyen CT, Bordas S, Heidarpour A. Modelling interfacial cracking with non-matching cohesive interface elements. *Comput Mech*. 2016;58:731-746. https://doi.org/10.1007/s00466-016-1314-y.
27. Gens A, Carol I, Alonso E. A constitutive model for rock joints: formulation and numerical implementation. *Comput Geotech*. 1990;9:33-20.
28. Carol I, Prat PC, López CMA. Normal/shear cracking model. Application to discrete crack analysis. *ASCE J Eng Mech*. 1997;123(8):765-773.
29. Caballero A, Willam KJ, Carol I. Consistent tangent formulation for 3D interface modeling of cracking/fracture in quasi-brittle materials. *Comput Methods Appl Mech Eng*. 2008;197:2804-2822. https://doi.org/10.1016/j.cma.2008.01.011.
30. Aliguer I, Carol I, Sture S. Stress-driven integration strategies and m-AGC tangent operator for Perzyna viscoplasticity and viscoplastic relaxation: application to geomechanical interfaces. *Int J Numer Anal Meth Geomech*. 2017;41:918-939. https://doi.org/10.1002/nag.2654.
31. Simo JC, Wriggers P, Taylor RL. A perturbed Lagrangian formulation for the finite element solution of contact problems. *Comput Methods Appl Mech Eng*. 1985;50:163-180.
32. El-Abbasi N, Bathe KJ. Stability and patch test performance of contact discretizations and a new solution algorithm. *Comput Struct*. 2001;79:1473-1486.
33. Rebel G, Park KC, Felippa CA. A contact formulation based on localized Lagrange multipliers: formulation and application to two-dimensional problems. *Int J Numer Meth Eng*. 2002;54:263-297. https://doi.org/10.1002/nme.426.
34. Zienkiewicz O, Taylor R. *The finite element method. Volume 1: The Basis*. 5th ed. Oxford, UK: Butterworth-Heinemann; 2000:346-364.
35. Schellekens JC, de Borst R. On the numerical integration of Interface elements. *Int J Numer Methods Eng*. 1993;36:43-66. https://doi.org/10.1002/nme.1620360104.

How to cite this article: de Francisco M, Carol I. Displacement-based and hybrid formulations of zero-thickness mortar/interface elements for unmatched meshes, with application to fracture mechanics. *Int J Numer Methods Eng*. 2020;1–27. https://doi.org/10.1002/nme.6562